Performance of the ATLAS Liquid Argon Endcap Calorimeter in the Pseudorapidity Region $2.5 < |\eta| < 4.0$ in Beam Tests

ATLAS Liquid Argon EMEC/HEC/FCAL Collaboration

J. Pinfold, J. Soukup

University of Alberta, Edmonton, Canada

J.P. Archambault, C. Cojocaru, M. Khakzad, G. Oakham, M. Schram, M.G. Vincter

Carleton University, Ottawa, Canada

V. Datskov, V. Drobin, A. Fedorov, S. Golubykh, N. Javadov [1], V. Kalinnikov, S. Kakurin, M. Kazarinov, V. Kukhtin, E. Ladygin, A. Lazarev, A. Neganov, L. Petrova, I. Pisarev, N. Rousakovitch, E. Serochkin, S. Shilov, A. Shalyugin, Yu. Usov

Joint Institute for Nuclear Research, Dubna, Russia

D. Bruncko, E. Kladiva, P. Stavina, P. Strizenec

Institute of Experimental Physics of the Slovak Academy of Sciences, Kosice, Slovakia,
Comenius University, Faculty of Mathematics, Physics & Informatics, Bratislava, Slovakia

F. Barreiro, C. Gabaldon, F. Labarga, E. Nebot, C. Oliver, S. Rodier [2], J. del Peso

Physics Department, Universidad Autonóma de Madrid, Spain

A. Belkin, M. Heldmann, L. Koepke, R. Othegraven, T. Schliephake, D. Schroff, H. Secker J. Thomas, C. Zeitnitz [3]

Institut für Physik der Universität Mainz, Mainz, Germany

Preprint submitted to Elsevier *18 April 2008*

C. Benchouk [4], F. Djama, F. Hubaut, E. Monnier, V. Niess, P. Pralavorio, M. Raymond, B. Resende, D. Sauvage [5], C. Serfon, S. Tisserant, J. Toth [6]

Centre de Physique des Particules de Marseille, Univ. Méditerranée, Marseille, France

G. Azuelos, P. Delsart, C. Leroy, R. Mehdiyev [1]

Université de Montréal, Montréal, Canada

A. Akimov, M. Blagov, A. Komar, A. Snesarev, M. Speransky, V. Sulin, M. Yakimenko [5]

Lebedev Institute of Physics, Academy of Sciences, Moscow, Russia

V. Epshtein, V. Khovansky, P. Shatalov,

Institute for Theoretical and Experimental Physics (ITEP), Moscow, Russia

M. Aderholz, T. Barillari, W. Cwienk, A. Fischer, J. Habring, J. Huber, A. Karev [7], A. Kiryunin [8], L.Kurchaninov [8,9], S. Menke, P. Mooshofer, H. Oberlack, D. Salihagic [10], P. Schacht

Max-Planck-Institut für Physik, (Werner-Heisenberg-Institut), Munich, Germany

T. Chen, J. Ping, M. Qi

University of Nanjing, Nanjing, China

V. Kazanin, V. Malyshev, A. Maslennikov, G. Pospelov [11], R. Snopkov, A. Soukharev, A. Talyshev, Y. Tikhonov

Budker Institute of Nuclear Physics, Novosibirsk, Russia

P. Cavalleri, P. Schwemling

Universites de Paris VI et VII, IN2P3-CNRS, Paris, France

S. Chekulaev, S. Denisov, V. Evdokimov, M. Levitsky, A. Minaenko, G. Mitrofanov, A. Moiseev [5], A. Pleskatch, D. Stoyanova, L. Zakamsky

Institute for High Energy Physics, Protvino, Russia

M. Bieri, D. O'Neil, J. Rani, D. Schouten, M. Vetterli [12]

Simon Fraser University, Burnaby, Canada

P. Loch, J. Rutherfoord, A. Savin, L. Shaver, M. Shupe

University of Arizona, Tucson, Arizona, USA

C. Galt, P. Gorbounov, N. Knecht, P. Krieger, L. Ma, R. Mazini, R. Orr

University of Toronto, Toronto, Canada

M. Losty, C.J. Oram, M. Wielers [13]

TRIUMF, Vancouver, Canada

P.S. Birney [14], M. Fincke-Keeler, I. Gable, T.A. Hodges, T. Hughes, T. Ince, N. Kanaya [15], R.K. Keeler, R. Langstaff, M. Lefebvre, M. Lenckowski, R. McPherson [16], W. Shaw

University of Victoria, Victoria, Canada

H.M. Braun, J. Thadome

University of Wuppertal, Wuppertal, Germany

Abstract

The pseudorapidity region $2.5 < |\eta| < 4.0$ in ATLAS is a particularly complex transition zone between the endcap and forward calorimeters. A set-up consisting of 1/4 resp. 1/8 of the full azimuthal acceptance of the ATLAS liquid argon endcap and forward calorimeters has been exposed to beams of electrons, pions and muons in the energy range $E \leq 200$ GeV at the CERN SPS. Data have been taken in the endcap and forward calorimeter regions as well as in the transition region. This beam test set-up corresponds very closely to the geometry and support structures in ATLAS. A detailed study of the performance in the endcap and forward calorimeter regions is described. The data are compared with MC simulations based on GEANT 4 models.

1 Introduction

Measurements of the energy and direction of electrons, photons and jets are the primary goal of the ATLAS calorimeter. In addition, missing transverse energy and particle identification are key issues for the calorimeter performance. In the past, calibration runs in beam tests have been carried out for individual set-ups of the electromagnetic (EMEC) [1–5], hadronic endcap (HEC) [6,7] and forward calorimeters (FCal) [8], and more recently for combined set-ups reflecting the ATLAS detector as closely as possible [9].

This beam test in the particularly difficult forward region $2.5 < |\eta| < 4.0$ (the transition from the electromagnetic endcap calorimeter EMEC and hadronic endcap calorimeter HEC to the forward calorimeter FCal) was carried out in 2004 and is a continuation of these calibration studies. The set-up had to be as close as possible to the final ATLAS detector, not only with respect to the calorimeter modules, but also with respect to the support structures and dead material distribution. It should be stressed that the set-up reproduced the ATLAS projective geometry at one $|\eta|$ point, but not over the entire $|\eta|$ region. The beam was incident at an angle of 4.2° onto the face of the calorimeters, corresponding to an average $|\eta|$ of 3.2. This tilt angle, which is correct on average but not for all $|\eta|$ impact positions, has no major impact on the hadronic response. The performance of electrons might be slightly affected.

The goal of this study is to obtain the hadronic calibration in the forward region $2.5 < |\eta| < 4.0$, including corrections for dead material effects. The analysis focused in particular on

---

[1] On leave of absence from IP, Baku, Azerbaijan
[2] Supported by the TMR-M Curie Programme, Brussels
[3] Now at University of Wuppertal, Wuppertal, Germany
[4] Now at Faculté de Physique, Université des Sciences et de la Technologie Houari Boumediène, Alger, Algérie
[5] deceased
[6] Also at KFKI, Budapest, Hungary, Supported by the MAE, the HNCfTD (contract F15-00) and the Hungarian OTKA (contract T037350)
[7] On leave of absence from JINR, Dubna, Russia
[8] On leave of absence from IHEP, Protvino, Russia
[9] Now at TRIUMF, Vancouver, Canada
[10] On leave of absence from University of Podgorica, Montenegro, Yugoslavia
[11] Now at Max-Planck-Institut für Physik, Munich, Germany
[12] also at TRIUMF, Vancouver, Canada
[13] Now at Rutherford Lab, Didcot, United Kingdom
[14] Now at CERN, Geneva, Switzerland
[15] Now at ICEPP University of Tokyo, Tokyo, Japan
[16] Fellow of the Institute of Particle Physics of Canada

(1) the intercalibration constants for and the performance of electrons and pions in the energy range $6\,\mathrm{GeV} < E < 200\,\mathrm{GeV}$ in the EMEC/HEC and FCal regions;
(2) a detailed comparison of electron and pion data with simulation to allow extrapolations to jets and a validation of the simulation programs based on the response to single particles;
(3) the energy corrections for electrons and pions when crossing the 'crack' between the two detector regions;
(4) the validation of the energy reconstruction in ATLAS using testbeam data. Here the assessement of systematic effects is of importance.

In this paper we cover the first two topics, the last two will be discussed in a forthcoming paper.

2 Set-up, Read-out and Calibration

2.1 Electromagnetic Endcap, Hadronic Endcap and Forward Calorimeters

The electromagnetic endcap calorimeter (EMEC) [10] is a liquid argon (LAr) sampling calorimeter with lead as absorber material. One endcap wheel is structured in eight azimuthal wedge-shaped modules. The accordion shaped kapton electrodes and absorber plates are mounted in a radial arrangement like spokes of a wheel, with the accordion waves running in depth parallel to the front and back edges of the module. The liquid argon gap between the absorber plates increases with the radius and the accordion wave amplitude and the related folding angle varies as a function of the radius. To keep the variation of the folding angle in a reasonable range, each endcap calorimeter consists of two coaxial wheels: an inner and an outer section covering a range of $1.375 < |\eta| < 2.5$ and $2.5 < |\eta| < 3.2$, respectively. The boundary between these two wheels is projective with the corresponding crack being about 3 mm wide. For this beam test a module of the inner wheel has been rebuilt using leftover electrodes available. Except for the missing outermost electrode in azimuth (ϕ), it corresponds exactly to a module from the series production.

The hadronic endcap calorimeter (HEC) [6,7] is a liquid argon sampling calorimeter with flat copper absorber plates, structured longitudinally in two separate wheels. Longitudinally each wheel has two read-out sections. The thickness of the absorber plates is 25 mm for the front wheel and 50 mm for the rear wheel. Each wheel is made out of 32 modules. In total 24 gaps (8.5 mm) for the front and 16 gaps for the rear wheel are instrumented with a read-out structure. Longitudinally the read-out is segmented in 8 and 16 gaps for the front, and 8 and 8 gaps for the rear wheel. The total number of read-out chan-

nels for a ϕ-wedge consisting of one front wheel module and one rear wheel module is 88. For the read out cold electronics [11] is used in HEC.

Due to the limitation in space, a special set of 8 front and 8 rear HEC modules has been built for this beam test. These had a reduced coverage in $|\eta|$, corresponding to $2.1 < |\eta| < 3.2$. Also the rear modules were of half size in depth, i.e. they had one rather than two longitudinal sections. But otherwise the modules correspond exactly to the modules of the series production, including cabling, support structures and read-out segmentation.

The forward calorimeters (FCal) [12] cover in ATLAS the region $3.1 < |\eta| < 4.9$. Starting about 4.7 m from the IP they are located within and concentric with the HEC. Each endcap is made of three modules, one behind the other, providing three depth segments. All modules have cylindrical electrodes made of a solid rod within a thin-walled tube. The gap between the rod and tube, maintained by a helically-wound PEEK fiber, fills with liquid argon. The gaps are small (0.250 mm, 0.375 mm and 0.500 mm for FCAL1, FCAL2 and FCAL3, respectively) in order to avoid excessive charge-buildup of the slowly drifting positive argon ions. The electrode axes run parallel to the beam over the depth of their respective module. The electrodes are embedded in a matrix in an hexagonal array. The electrode rods, tubes, and matrix of the electromagnetic module are made of copper. The next two modules are hadronic calorimeters. Their electrode rods are solid tungsten, the tubes are copper, and the matrix is scintered tungsten alloy. At each end of these modules a copper plate holds the electrodes in place.

The FCal modules used in this beam test are engineering prototypes of the FCAL1 and FCAL2 ATLAS modules and are those used in the 1998 beam tests [8]. Each module is full-scale and nearly identical to the ATLAS modules except they correspond to $\pi/2$ ϕ-slices. These were oriented so that the ϕ coverage extended to $\pm\pi/4$ to the vertical. For the first module the electrodes extend only over the ϕ range $\pm 3 * \pi/16$ leaving an uninstrumented section of $\pi/16$ at each ϕ boundary. Because no engineering prototype of the third module was available, a conventional liquid argon calorimeter with parallel copper plates as absorbers and 2 mm double planar gaps was built (cold tailcatcher, CTC). The readout segmentation was 2×8 and 8×2 (in η and ϕ) at each gap to give stereoscopic position information. The eight double gaps were ganged in depth in the readout.

Fig. 1 shows a schematic diagram of the set-up in ATLAS. In particular the support structures are shown as black regions. In the beam test these structural parts have been realized in detail, except for the cryostat walls in front of the whole set-up: here the ATLAS endcap cryostat walls correspond to 0.90 radiation lengths ($X_\circ$) and the beam test cryostat walls to 0.31 $X_\circ$. Of particular importance is the projective support in front of FCAL1 centered at

$|\eta| \simeq 3.2$.

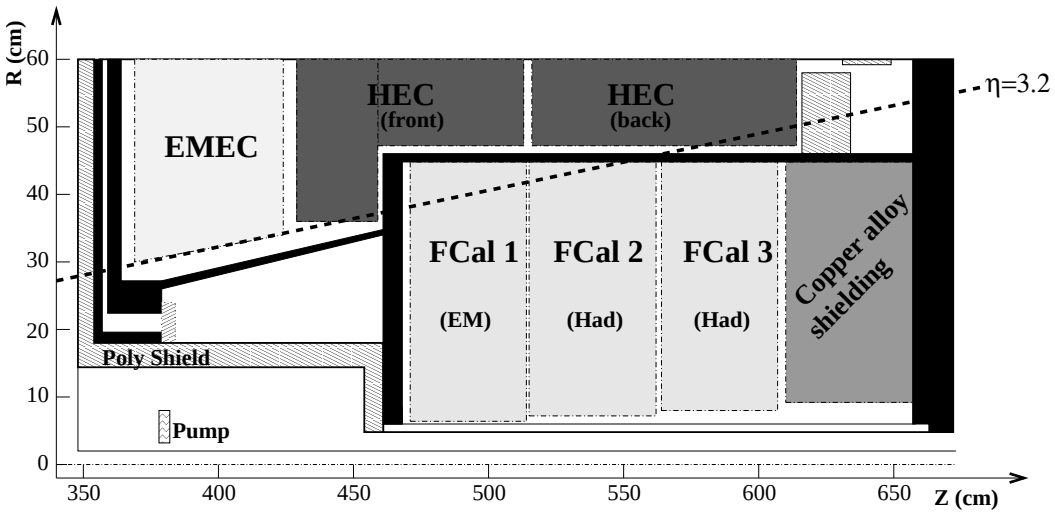

Fig. 1. Schematic diagram showing the transition in ATLAS from the EMEC and HEC calorimeters to the FCal calorimeter. All additional support structures and cryostat walls are shown as well (black regions).

2.2 Warm Tail Catcher

A warm tailcatcher calorimeter (WTC) has been added in the beam test set-up to correct for residual longitudinal leakage due to the reduced longitudinal coverage of the HEC calorimeter (last longitudinal section missing) with respect to ATLAS. The WTC is located immediately behind the cryostat and consists of steel plates interleaved with scintillation counters as active elements. In total four steel plates, each 10 cm thick, 125×125 cm^2 in area and separated by 5 cm, are used as absorber. The active elements are six layers of scintillation counters (1.27 cm thick), two layers in front of the first absorber plate and one layer immediately behind each absorber plate. The first two layers are structured in six, all others in three scintillation counters with either horizontal or vertical orientation. The first two layers (vertical and horizontal orientation) are intended to allow for corrections for the energy losses in the cryostat wall. Each scintillation counter is read out via a wavelength shifter bar with a photo-multiplier tube (PMT) at each end. Thus a rather uniform response of the light collection has been achieved. Studies using a wide muon beam show that the uniformity in response achieved is typically at the level of ± 10 %. The normalization of each PMT has been obtained using the muon response.

The beam tests have been carried out in the H6 beamline at the CERN SPS, which provides hadrons, electrons or muons in the energy range 6 GeV $\leq E \leq$ 200 GeV. The data have been taken in two run periods in 2004.

Two operation modes of beams have been used, one with a narrow beam, typically with a width σ less than 1 cm, and the other one with a wide beam with a width σ of typically a few cms. At the nominal impact points (see Fig. 8) either a grid of 1 cm has been scanned around the center with the narrow beam or one data set has been taken with the wide beam. In each case the total statistics was kept at the same level. Thus potential local detector variations have been averaged, a particularly important issue for the FCal (see [8]).

The general set-up with the most relevant beamline elements is illustrated in Fig. 2. The particle trigger was based on the coincidence of three scintillation

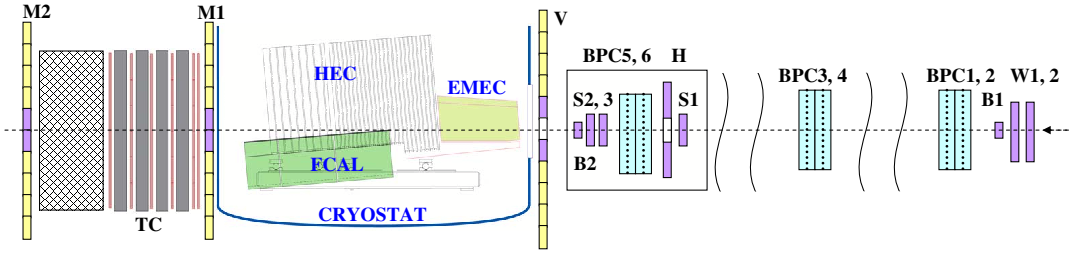

Fig. 2. Schematic view of the general beam test set-up. Shown are the modules in the cryostat as well as the beam instrumentation used: multiwire proportional chambers (BPC), scintillation counters (S, B) and scintillator walls (V, M1, M2) The beam moves from right to left.

counters S1, S2 and S3, which were in size 10×10 cm^2 (S1, S2) and 7.5×7.5 cm^2 (S3). For the narrow beam option a smaller scintillation counter (2×2 cm^2), B2, could be added to the coincidence. The selection of the narrow or wide beam option was done by the DAQ software on request from the operator. A veto scintillation counter with a beam hole of 6 cm diameter was positioned right behind S1 to tag beam halo particles. To be able to adjust for the various vertical beam positions, these counters - as well as the beam chambers - were mounted on a vertically movable table. In addition three scintillator walls V, M1, M2 were used in the trigger selection: the veto wall V was located right in front of the cryostat, the muon trigger walls were behind the cryostat and behind the beam dump of the H6 beamline. The M1 and M2 scintillator walls were separated by an iron wall. Muons are tagged using the coincidence of M1 and M2 signals. Up to beam energies of 80 GeV the Cherenkov counter

was used for particle selection. The data from the veto counter, veto wall V, muon walls M1 and M2 and the Cherenkov counter have only been recorded by the DAQ, but not used in active trigger. Thus any bias in the data sets has been avoided, but the information has been used in the offline analysis to make detailed unbiased studies of various issues such as beam contamination, optimization of trigger selection for different beam conditions, and background studies.

The impact position and angle of beam particles were derived using hit information from 6 multiwire proportional chambers (BPC-1 - BPC-6), each with a vertical (y) and horizontal (x) read-out plane. The read-out was based on a cathode delay line scheme, one for each plane, i.e. 12 in total. The chambers were positioned at three tracking stations, with two x and two y planes per station. The far station (BPC-1, BPC-2) with planes with 150 μm position resolution were placed next to the vertical bending magnet, about 30 m upstream of the cryostat. The second station (BPC-3, BPC-4, 300 μm position resolution) was about 19 m upstream of the cryostat, located on a second vertically adjustable table. The last station (BPC-5, BPC-6, 150 μm position resolution) was in front of the cryostat, at a distance of about 3 m, on the same vertically movable platform as the trigger counters.
The gas used was a mixture of argon and CO_2, the detection efficiency was almost 100%. Each plane had an analog amplitude measurement and two logical outputs (two ends of delay line) for the position measurement via a CAMAC TDC. The close proximity of planes in each station allowed consistency checks reducing thus the effect of delta-electrons on the position measurement. In addition, the TDC checksum has been used at each plane to exclude 'multi track' events.

The positions of the BPC wire planes along the beamline were surveyed prior to the beam test. Track fits were performed separately in the $x-z$ and $y-z$ planes. Average track residuals calculated run-by-run for the full run period are typically below $\sim$ 200 μm, in both coordinates. This tracking system allowed determination of the particle impact angle with a precision of $\sim$ 10 μrad and the impact point with a precision of $\sim$ 100 μm (at high energies). The combination of angular and position measurements allowed suppression of the beam contamination due to upstream scattering of particles and improve also the e/π separation for secondary beam settings (e.g. high energy electrons).

Finally, a scintillation counter B1 in front of two multiwire proportional chambers (W1, W2) with vertical and horizontal planes per chamber having 1 mm wire spacing triggered the read-out of these chambers independently of the beam trigger and enabled thus detailed information on beam profiles at large scale.

The cryostat has an inner diameter of 2.50 m and may be filled with liquid

argon (LAr) up to a height of 2.20 m. It can be moved horizontally by ± 30 cm perpendicular to the beamline. The beamline vertical bending magnet allows vertical deflection of the beam by ± 25 cm at the front face of the cryostat. In this beam region a circular cryostat beam window of 60 cm diameter has a reduced wall thickness (5.5 mm stainless steel). Thus an area of $60 \times 50\,\mathrm{cm}^2$ is available for horizontal and vertical scans.

The load in the liquid argon cryostat consists of the inner section of one EMEC module (in ϕ 1/8 of the full EMEC wheel), eight specially constructed front wheel HEC modules (8/32 of the full wheel), eight purpose-built rear wheel HEC modules and the FCal modules. Constrained by the cryostat dimensions the depth of the rear wheel HEC modules was half of the ATLAS modules. Again, due to the limited space available, the HEC modules were of reduced radial size, covering the region of interest $2.1 < |\eta| < 3.2$.

The region available for vertical (i.e. η) scans is rather limited due to the bending power of the last magnet and the size of the cryostat window. Therefore data have been taken in two run periods with different vertical positions of the cryostat: the cryostat position was lower by 13 cm in the first run period. In addition, a second bending magnet (located just upstream of the first) has been added for the second run period.

Fig. 3 shows a schematic of the set-up of the different calorimeter modules (second run period). The beam enters through the cryostat window from right at a nominal position of $y = 0$ cm. Shown are the inner EMEC (front), the HEC front wheel and rear wheel modules as well as the FCal1 and FCal2 modules (below the HEC modules). In addition a cold tailcatcher (CTC) is placed right behind the last FCal module in order to measure any leakage beyond the FCal2 module. In a similar way the energy leakage for the rear wheel HEC modules is measured in a warm tailcatcher (WTC) placed outside the cryostat. The loading of the cryostat with the full assembly of all calorimeter modules is shown in Fig. 4. Seen is the EMEC module (right) with LAr excluders on top and bottom as well as the forward cone (cold wall) of the FCal, which in ATLAS extends the tube to the front face of the cryostat (below the EMEC, for details see Fig. 1) and the HEC modules with the electronic boards on top. The FCal modules are below the HEC, to a large extent hidden behind the support frame structure. Two LAr excluders are visible: on top of the EMEC module the excluder in front of the HEC modules, and on bottom the excluder in front of the FCAL1. The exact positioning of the excluders in combination with the residual LAr adds some uncertainty to the $|\eta|$ dependence of the distribution of inactive material in front of the calorimeters. The restrictions of the set-up in space obviously have an impact on energy leakage beyond the acceptance. The longitudinal energy leakage for pions depends on the beam energy and is typically at the level of 2-4 % (see section Monte Carlo simulation section 4). This leakage can partially be recovered using the tail catcher signals. The

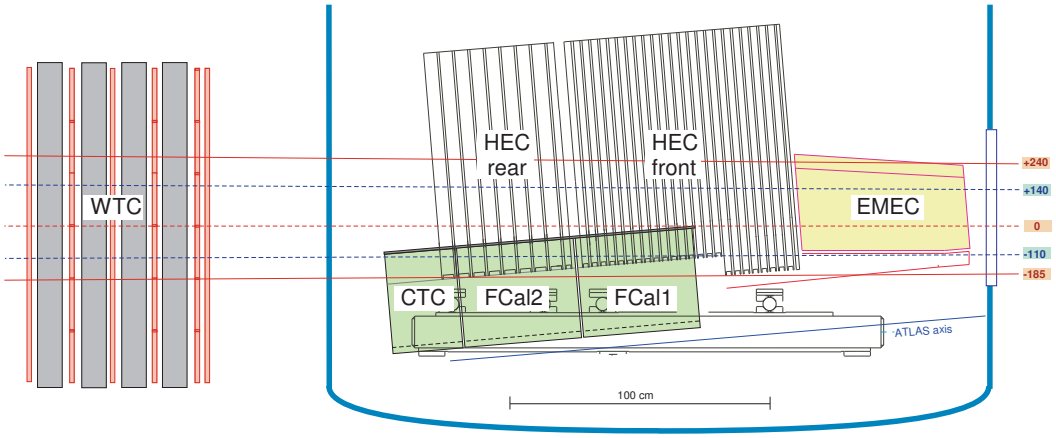

Fig. 3. Schematic view of the calorimeter set-up. Shown are the inner EMEC (front), the HEC, the FCal1 and FCal2 modules (below the HEC modules). In addition, the cold tailcatcher (CTC, behind FCAL2) and the warm tailcatcher (WTC, outside of cyostat) are shown as well.

lateral leakage strongly depends on the impact point chosen, therefore a direct comparison to MC simulation is essential for any conclusions.

Monitoring of the LAr purity and temperature is done as in previous beam tests. For details see e.g. [6].

2.4 Read-out Electronics and Data Acquisition

The block diagram of the front-end and read-out electronics is shown in Fig. 5. The output signals of the HEC cold electronics [11] as well as the raw signals from the EMEC and FCal were fed to front-end read-out boards (FEB) outside the cryostat, where they are amplified, shaped and sampled in time with the TTC clock. The samples are stored in the switched capacitor array of the FEB at a rate of 40 MHz. The crate with the FEBs was directly located on the two related feedthroughs as in the ATLAS set-up. After arrival of the event trigger the sampling was stopped, the signals were digitized and transfered to the read-out driver via a serial link. The read-out was performed by eight MINI-ROD modules, exploited previously for the EMEC tests [4] and FCAL tests [8].

The triggering and the synchronization of the eight FEBs, the eight MINI-RODs and the three calibration boards were done using the TTC-0 system as employed in the EMEC tests (see e.g. [4,13]). The MINI-ROD read-out was based on VME. A CAMAC crate was employed in the data acquisition system as well. This crate covered the read-out of the two TDC modules to get the time difference between the event trigger and the 40 MHz ADC clock, as well as the read-out of the 'multi wire' proportional chambers and scintillation

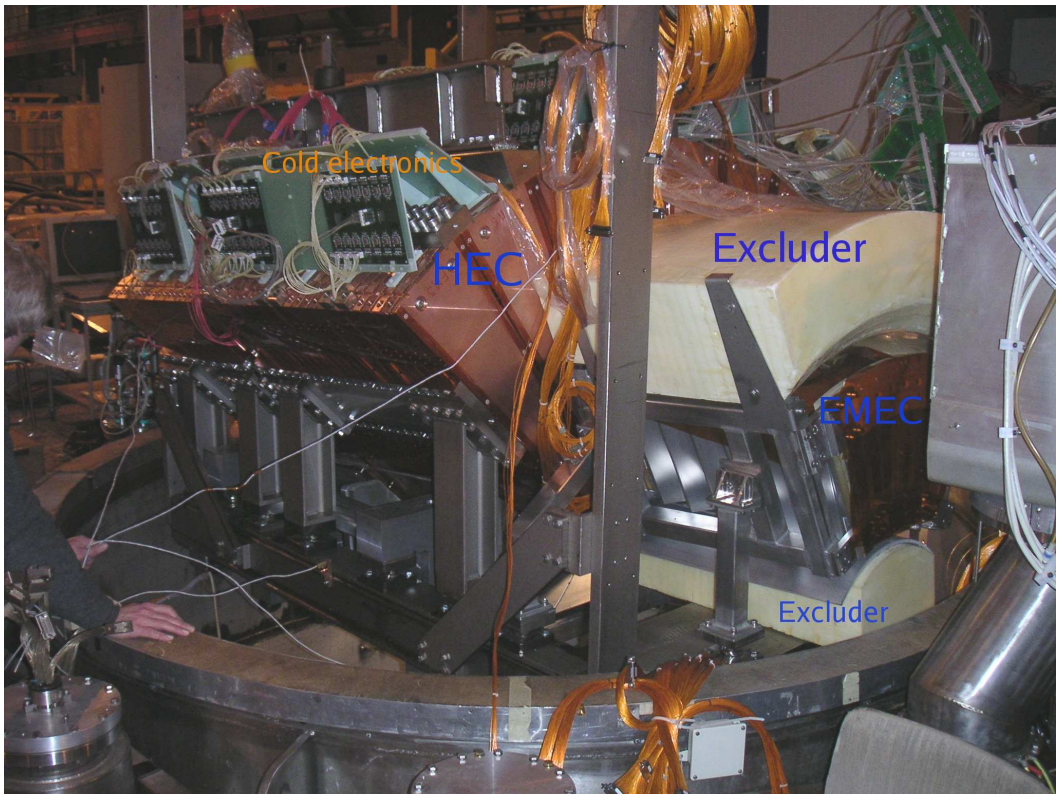

Fig. 4. Loading of the cryostat: shown is the EMEC module (right) with the LAr excluders on top (in front of HEC1) and bottom (in front of the FCAL1) as well as the cold wall of the FCal (below the EMEC) and the HEC modules with the electronic boards on top. The FCal modules are below the HEC and to a large extent hidden behind the support frame structure.

counter registers. The VME crate was connected via an optical link (Bit3) to a PC running under LINUX where all data have been monitored and finally written to disk.

2.5 Calibration

The data are read-out every 25 ns as will be the case during normal ATLAS operations. Typically seven samples have been read-out with the first one right on the baseline. Five samples have been used to reconstruct the signal amplitude. The signal amplitude has been reconstructed using the optimal filtering method [14–17] as foreseen for ATLAS and as tested in previous beam tests [9]. Some special runs with 32 samples have been taken to study signal shapes in more detail.

The hardware calibration system was as used as in previous runs (see e.g. [9]). The calibration pulse is injected directly at the electrode read-out for the HEC, at the boards positioned at the module backplane (motherboards) for the

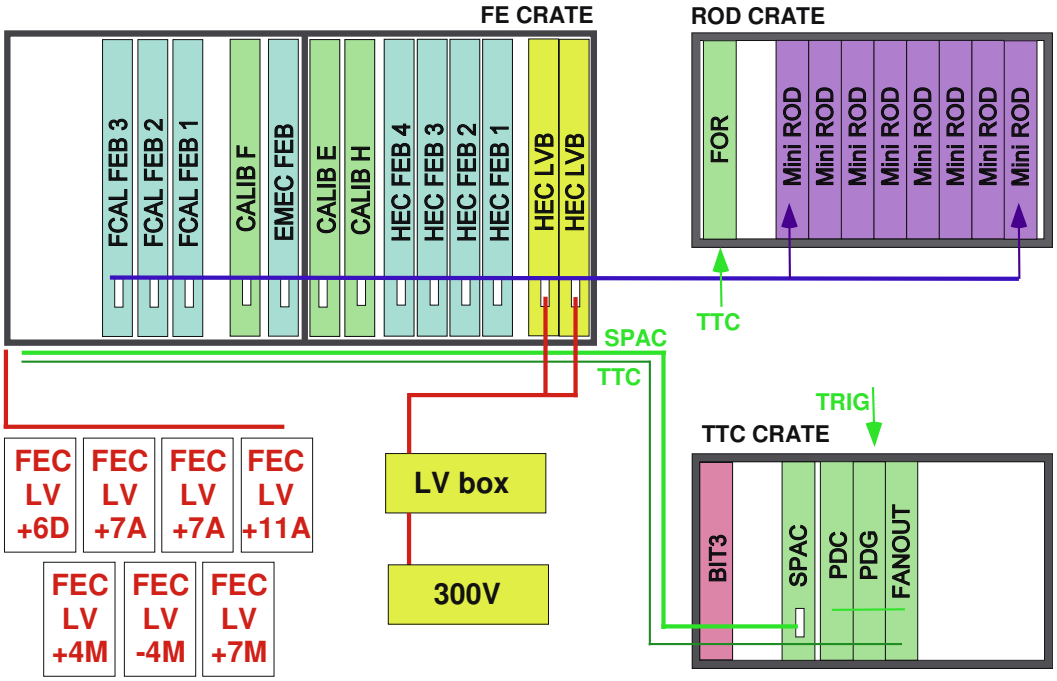

Fig. 5. Block diagram of the front-end and read-out electronics.

EMEC and at the front-end crate for the FCal. Therefore somewhat different calibration procedures have been used for the three calorimeter systems. For details of the EMEC and HEC procedures see [9] and of the FCal procedure (see [12]).

2.5.1 HEC calibration

For the HEC, the calibration signal is input at the pad level, very closely to the real signal input. To test the quality of the signal reconstruction the waveform was obtained by averaging the experimentally measured signal samples which were divided by the signal amplitude A_{OF} reconstructed using the optimal filtering approach (OF) [15]. The beam particles arrive asynchronously with respect to the 40 MHz clock, the relative phase is measured with a TDC. Therefore only a fraction of the pulses are sampled near the peak. The expected reconstructed pulse height is defined to be that of an ideal continuous pulse passing through these samples. The quality of the signal reconstruction can be assessed by taking a large number of events with hits in a channel, and plotting the average value of the sample in a given time bin normalized event-by-event to the reconstructed pulse height. Because this average pulse is reconstructed for many pulses with different sampling times, the complete average pulse can be reconstructed with fine time bins. This is shown in Fig. 6 for a typical HEC channel for pions of 200 GeV. The position and the value of the maximum as indicated in the figure are obtained from a parabolic fit in the region of the maximum. If the reconstruction based on the optimal

filtering technique works perfectly then the observed height of this normalized distribution should be unity. The waveform is shown for large signals (signal/$\sigma_{\text{noise}} > 50$) and small signals ($5 \leq$ signal/$\sigma_{\text{noise}} \leq 15$) to demonstrate that the OF reconstruction works equally well in both regions, i.e. for different cell positions in the hadronic shower. As can be seen, the maximum in both cases is very close to unity.

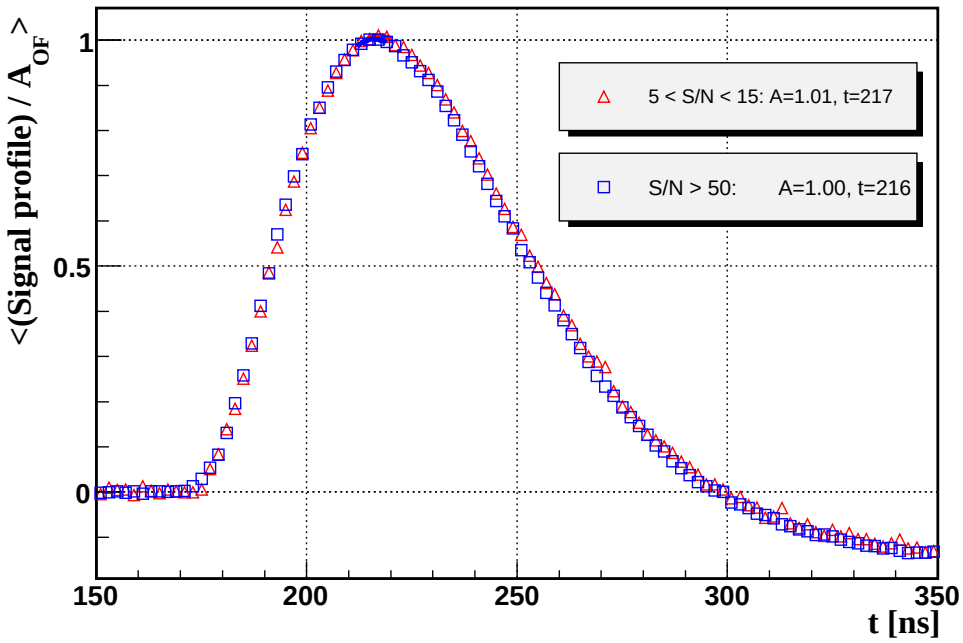

Fig. 6. The measured signal in a typical HEC channel for pions of 200 GeV. Shown are the measured signals (five time slices per event) relative to the reconstructed amplitude using the optimal filtering technique. The waveform is shown for large signals (signal/$\sigma_{\text{noise}} > 50$) and small signals ($5 \leq$ signal/$\sigma_{\text{noise}} \leq 15$).

2.5.2 EMEC calibration

For the EMEC the calibration signal is input at boards at the back of the module. The ratios of the measured and reconstructed amplitudes have been studied for the EMEC channels in a similar way as for the HEC channels [16,17] (see above). Fig. 7 shows these ratios of the real amplitude relative to the reconstructed amplitude using the optimal filtering technique for different EMEC channels. The values are shown for large signals (signal/$\sigma_{\text{noise}} > 50$) and have been obtained (as explained in Fig. 6 for the HEC case) for electrons of 150 GeV. The RMS of the distribution is 1.5 %.

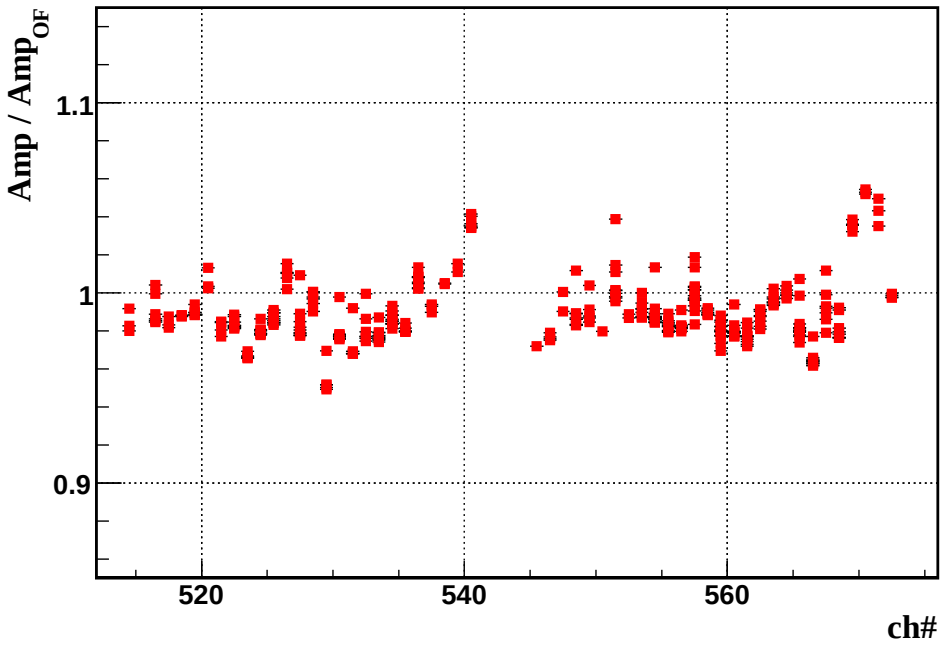

Fig. 7. The ratio of the real amplitude to the reconstructed OF amplitude for electrons of 150 GeV in several EMEC channels. The RMS of the distribution is 1.5 %.

2.5.3 FCal calibration

For the FCal, the calibration pulse is introduced at the baseplane of the front end crate far from the calorimeter electrodes. At the injection point half of the current pulse goes directly to the warm preamplifier and is used to calibrate the electronics. The other half goes down the signal cable, reflects off the electrodes, and returns to the warm electronics well after the first half. This reflected pulse provides diagnostic information for the cold electronics chain. For those special calibration runs where 32 time samples have been read out, both halves of the calibration pulse have been recorded. For the conventional calibration runs with seven time samples only the direct pulse is seen.

3 Data Analysis

3.1 Data

In the two run periods more than 4000 runs have been taken with electrons, pions or muons in the energy range $6\,\mathrm{GeV} \leq E \leq 200\,\mathrm{GeV}$ with about 80 million triggers in total. Energy scans have been taken at a standard set of

impact points. In addition, horizontal and vertical scans have been done at fixed particle energies. The distribution of impact points and scan lines on the front face of the calorimeter is shown for the second run period in Fig. 8. The read-out structure for the various calorimeters as well as the projection of the cryostat window on the calorimeter front face are shown as well. The frequently used impact points D and H for the EMEC/HEC and FCal data correspond to $\eta = 2.8$ and $\eta = 3.65$ in ATLAS. We focus in this paper on the electron and

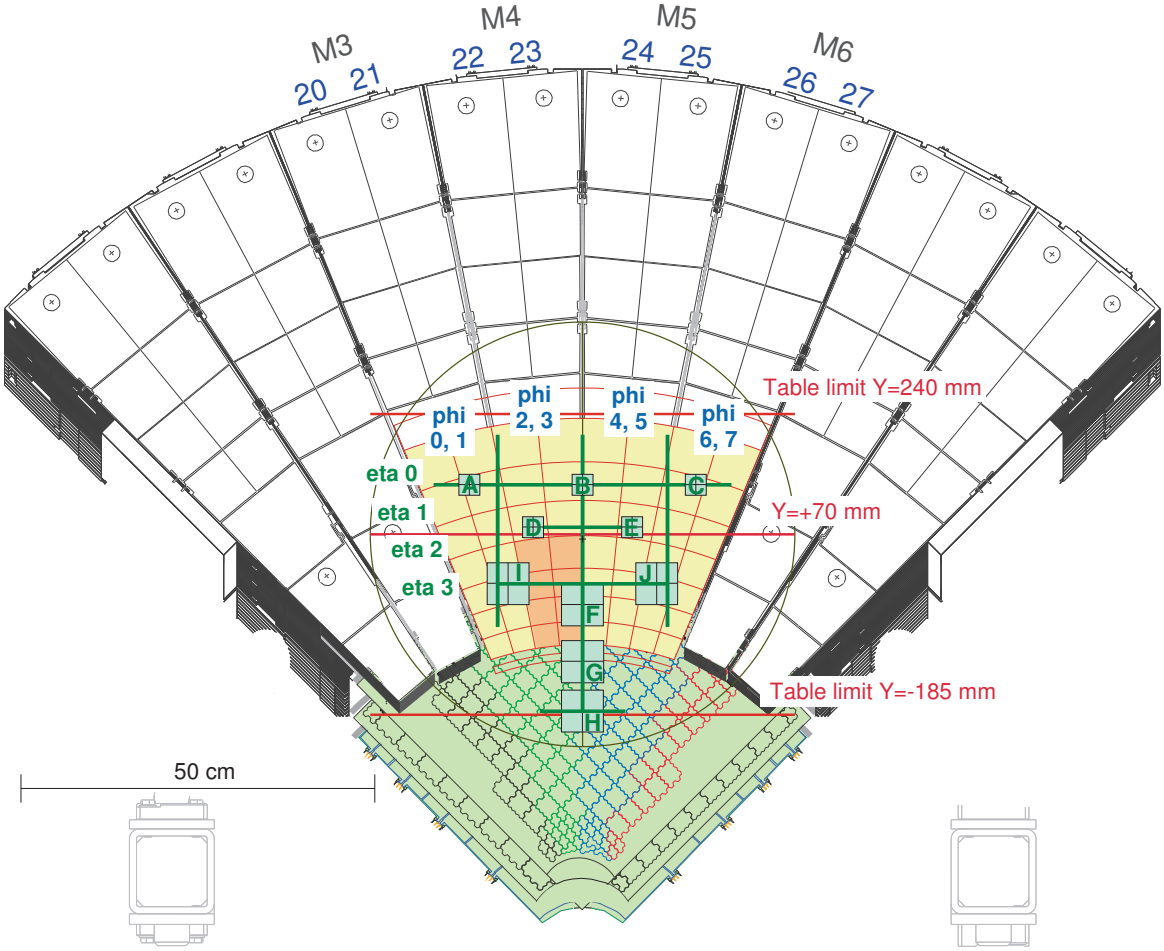

Fig. 8. Position of the beam impact points and scan lines on the front face of the calorimeter. The squares indicate the region scanned for the data taken at the nominal impact points. The lines indicate the horizontal and vertical scans where the data have been taken at fixed energies.

pion performance results in the EMEC/HEC and FCal regions. First results from the vertical scan covering the full crack region are given as well. Here it is only relevant to compare the data with MC simulation in order to verify the geometry and inactive material distribution. Even in the restricted fiducial regions the effects of the crack between the calorimeters are affecting the performance at a lower level. This is particularly true for the pion data. In a forthcoming paper we will address the full energy reconstruction including the dead material corrections as foreseen in ATLAS [19]. Throughout the paper

the mean signal and the resolution σ have been obtained from a Gaussian fit in the region of ± 2 RMS around the mean of the distribution.

3.2 Signal Reconstruction

The signal of the particle response has been reconstructed using a number of different approaches.

To extract the basic information on the calorimeter performance a rather simple approach has been chosen. Here one sums all signals around the impact point within a cone R in $\Delta\eta \times \Delta\phi$. A cell is added to the cluster if the distance between its center and the barycenter of the cluster is less than or equal R. The cluster finding algorithm is converging very fast, typically not more than 2-3 iterations are required. The cone size has been varied, in particular when going from electron data to pion data. Obviously a larger cone size adds more noise to the signal but reduces any out-of-cluster leakage. The fixed cone size allows also a straightforward noise subtraction for a given run, an important issue when the noise is not constant in time. In the cone approach the electromagnetic scale has been obtained normalizing the cluster energy for high energy electrons and cone size $R = 0.25$ to the related beam energy. Whenever possible, the average for few impact points has been used.

To compare the cone reconstruction with more sophisticated noise suppression schemes also a variant with additional σ cuts has also been employed. Here only cells are kept where the signal is above some given threshold with respect to the cell noise expectation (σ).

An electron reconstruction using fixed size clusters based on 3x3 and 5x5 cells has been used as well and compared with the cluster reconstruction based on a given cone size in $\Delta\eta \times \Delta\phi$. This method is widely used in ATLAS and allows a straightforward comparison to the results from previous EMEC beam tests (see e.g. [4]). In this scheme the final corrections due to the residual η variation and ϕ modulations as well as the out-of-cluster leakage as expected for electrons in the EMEC calorimeter have been taken into account (see following text). These corrections are at the level of $1 - 2\%$ and relevant only for electrons. The ATLAS acceptance for high precision electron and photon reconstruction extends only up to $|\eta| < 2.5$, i.e. does not cover the inner EMEC wheel.

In a second approach the signal reconstruction has been done in a similar way as foreseen for ATLAS to obtain more information on the finally expected performance. Here a topological cluster reconstruction, based on geometrical information of neighbouring cells, is being used. This method starts with a seed cell above some threshold with respect to the σ of the cell noise level (n_1). This

center is expanded in three dimensions adding neighbouring cells which again are above a second threshold level (n_2). Clusters with common neighbours are merged and vice versa clusters with substructure may be split. Finally perimeter cells above a third threshold (n_3) are added. Thus the topological clustering is defined by three parameters ($n_1/n_2/n_3$). In this method the signal size is optimized with respect to the noise level on an event by event level. The topological clustering is planned for use in ATLAS for the reconstruction of the hadronic energy. Any noise subtraction, as required to extract the calorimeter performance parameters, is not trivial, in particular when the noise is not constant in time. A typical parameter set used in MC studies covering the full η acceptance in ATLAS is 6/3/3 σ for electrons and 4/2/0 σ for pions. In particular the parameter n_1 is obviously a compromise between noise reduction and signal loss.

3.3 Noise

For the HEC cold electronics a prototype of the final low voltage system has been used. It was noticed that the filter at the output stage was not efficient enough to suppress the typical noise from the DC/DC converter stage. The HEC data therefore show a coherent noise with a typical frequency of 163 kHz. Looking at the phase difference between a reference channel and all others it was found that the phase difference is either 0 or π. Using this fact, a global fit for all channels has been carried out and the noise amplitude for all channels has been obtained.

To correct the data, the phase difference for each individual event has been determined using the sum of all HEC channels (far from the beam impact point) taking into account the relative phase difference of 0 or π. Thus a correction for this noise has been obtained.

After correcting for these oscillations, additional, but substantially smaller, noise contributions have been observed in the data. These were not constant with time, and were also partially coherent. During the time when calibration data were taken, these additional noise contributions were rather small. Therefore they were not immediately detected. In order to properly account for this, the noise subtraction has been performed using random trigger events selected from the same runs as the physics data. For each run clusters using identical read-out cells as used for the real data have been reconstructed from the random trigger events.

In a first step this approach has been tested. Using runs where the beam impact point is far away, i.e. where the cluster contains empty cells only, this method can be tested by comparing the empty cluster with the cluster from

random trigger events. For this test the list of cells used in the cluster has been kept fixed. Fig. 9 shows this comparison for a typical electron cone size of $R = 0.15$ for the EMEC. The larger statistic is obtained for the real events, the smaller for the random trigger events. The histogram shows the data, the line a fit to the data assuming a gaussian distribution. The noise distributions agree rather well, obviously the mean is zero and the σ values are close within errors. A similar comparison for the same cells is shown in Fig. 10 but for a run in a different run period. Again, the agreement between the noise distributions is rather good, but they differ substantially from the noise in Fig. 9. This shows clearly the time dependence of the noise performance.

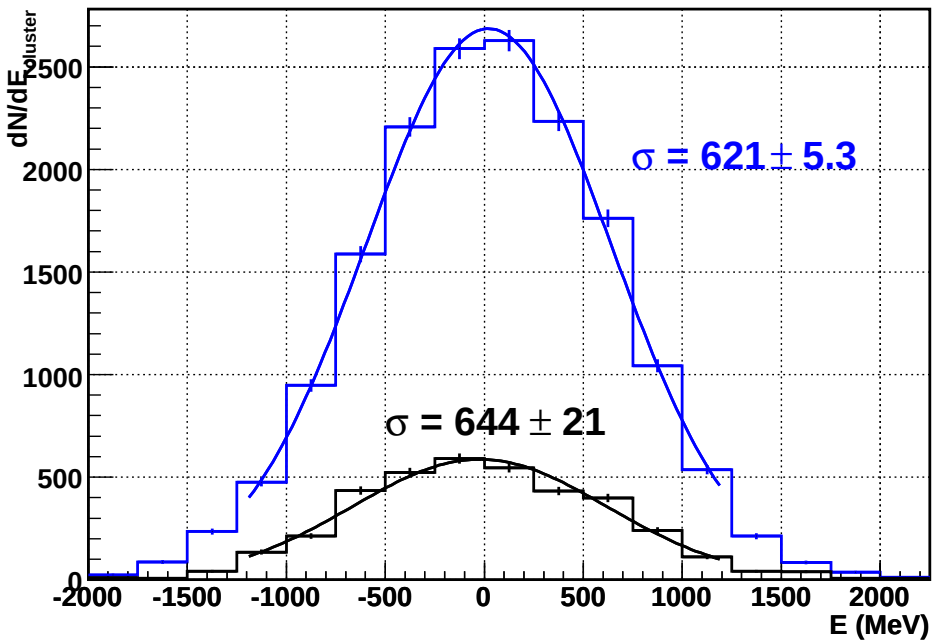

Fig. 9. Noise distribution (electromagnetic scale) in the EMEC for a cone of size $R = 0.15$. The cone has been reconstructed from data where the beam impact point was far off (large statistics) or constructed from random trigger events (small statistics). The agreement is rather good.

Based on these results the noise subtraction for the data has been done finally using the exact list of read-out cells in a data cluster for the next random trigger event in the same data file. Thus for the noise estimate a close correlation to the real event with respect to time and actual cluster is kept.

Finally, Table 1 shows the typical noise, in MeV, at the appropriate electromagnetic scale, for cells in the different longitudinal sections of the three calorimeter systems. Table 2 shows the corresponding mean reconstructed noise, for a number of different cone sizes R. For the electromagnetic sections of the EMEC and FCal, the noise is reconstructed at the electromagnetic scale,

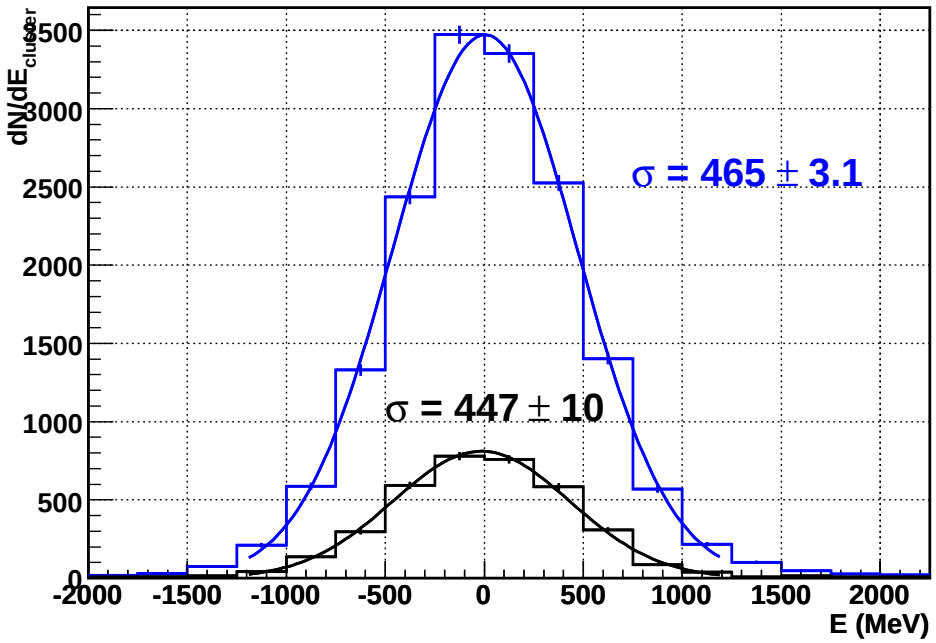

Fig. 10. Noise distribution (electromagnetic scale) in the EMEC for a cone of size $R = 0.15$. The cone has been reconstructed from data where the beam impact point was far off (large statistics) or constructed from random trigger events (small statistics). The agreement is rather good.

using cone sizes appropriate for electromagnetic clusters. The lower half of the Table shows the reconstructed noise expected for the reconstruction of pion data. These use the larger cone sizes more appropriate to hadronic reconstruction and sum over all longitudinal sections. These results, in GeV, have been calibrated to the hadronic energy scale.

Calorimeter section	**Mean Cell Noise [MeV]**	**expected Cell Noise [MeV]**
EMEC2	80	80
EMEC3	60	60
HEC0	200	190
HEC1	280	250
HEC2	460	420
FCAL1	240	180
FCAL2	370	315

Table 1
Example of typical mean cell noise (MeV) on the electromagnetic scale

Calorimeter	**cone $R = 0.15$**	**cone $R = 0.25$**	
EMEC [GeV]	0.55	1.3	
FCal [GeV]	0.59	1.1	
	cone $R = 0.30$	**cone $R = 0.40$**	**cone $R = 0.50$**
EMEC/HEC [GeV]	4.2	5.6	7.1
FCal [GeV]	3.1	4.6	6.7

Table 2
Example of mean noise (GeV) in typical cone for electrons ($R = 0.15$ and $R = 0.25$) and hadrons ($R = 0.30$, $R = 0.40$ and $R = 0.50$). The energy is given on the electromagnetic scale for electrons and on the hadronic scale for hadrons.

4 MC Simulation

One of the goals of these beam test studies is to extract calibration constants from the beam test data and transfer them to the final ATLAS detector. However, in ATLAS the final hadronic calibration is driven by jets rather than single particles. Therefore the use of MC simulation and the validation of the MC in beam tests (see e.g. [18]) is of utmost importance. The first step in this process is the comparison of the data with MC simulation at the electromagnetic scale. This scale is the basis for any hadronic calibration (see e.g. [19]) approach. Next in priority are studies of shower shape parameters and fluctuations, which might have an impact on hadronic weighting algorithms. Finally, given the rather limited acceptance of the beam test set-up any energy leakage needs to be understood prior to drawing conclusions from the comparison of the data with MC expectations.

Previous studies were mainly devoted to a comparison of the data with MC in EMEC, HEC and FCal stand alone runs or in the EMEC/HEC combined set-up at lower η. The high η region is affected by different read-out and dead material structures and is studied in this beam test for the first time. In particular with the detailed realization of the transition region at $|\eta| = 3.2$ this beam test analysis allows for the first time a realistic comparison of the data with MC almost over the full acceptance region $2.5 < |\eta| < 4.0$.

To compare data with MC expectation the simulation code GEANT 4 [20], version 7.1 has been used. Within this process the validation of the physics models in GEANT 4 is one of the most important tasks. From the physics lists for hadronic shower simulations available in GEANT 4 the physics lists QGSP-GN 2.6 and QGSP-BERTINI 2.6 have been used. The QGSP physics list is based on theory driven models: it uses the quark-gluon string model for interactions and a pre-equilibrium decay model for the fragmentation. The

range threshold for production has been set to 30 μm in general, irrespective of the material.

One of the known shortcomings of the QGSP-GN option is that the shower size is somewhat more compact in the simulation than seen in the data (see [18]). The QGSP-BERTINI option is expected to increase the shower size somewhat in comparison to the QGSP-GN version and thus should give a better description of the shower shapes. Therefore both options have been used for the study of the pion shower shape.

5 Electron Results

5.1 Electrons in EMEC/HEC Region

5.1.1 η-dependent Correction

Because of the EMEC geometry and the projective high voltage (HV) sectors, the electron response varies with η [4]. For the inner wheel (used in this set-up) there are two η regions with constant HV: $2.5 < |\eta| < 2.8$ and $2.8 < |\eta| < 3.2$. To correct for the slope of the response inside HV sectors an η dependent correction has been applied to each read-out cell. A parameterization, which has been found to be optimal [4], is

$$E_{corr} = E_{cell} \cdot \frac{\beta}{1 + \alpha \cdot (\eta_{cell} - \eta_0)} \tag{1}$$

where η_0 is the center of the related HV sector and α and β are free parameters. Given the relationship between high voltage, drift time and EMEC geometry, one expects α to be in the range $0.4 - 0.5$ and β should be close to 1 (for details see [21]). To obtain these parameters vertical (i.e. η) scans of electrons of 193 GeV and 119 GeV have been studied, using a cone of $R = 0.25$. MC studies show that the leakage outside this cluster is negligible. The values obtained are $\alpha = 0.55$ for both HV sectors and $\beta = 1.0$ (1.04) for the low (high) η section.

These corrections have been applied to the data. Then the above fit has been repeated, but for a smaller cone size ($R = 0.15$) just to crosscheck the corrections on a finer η scale. If the correction were perfect values of $\alpha = 0$ and $\beta = 1.0$ are expected. Because of the small leakage outside the cluster, the value of β obtained is slightly less than one whereas α is now compatible with 0 within errors. The results are unchanged when varying either the electron energies or the x (i.e. ϕ) position of the vertical scan. As an example Fig. 11 shows the result for a vertical scan with electrons of 193 GeV. Shown is the response, after correction for the η dependence, for the total cluster energy. In addition at each impact point all individual cell signals above 5% of the total signal are shown as well. This makes the cell boundaries in y evident and shows the most prominent individual contributions to the total signal. The shown cells belong obviously to two central adjacent ϕ strips which share most of the cluster energy in an approximately equal ratio.

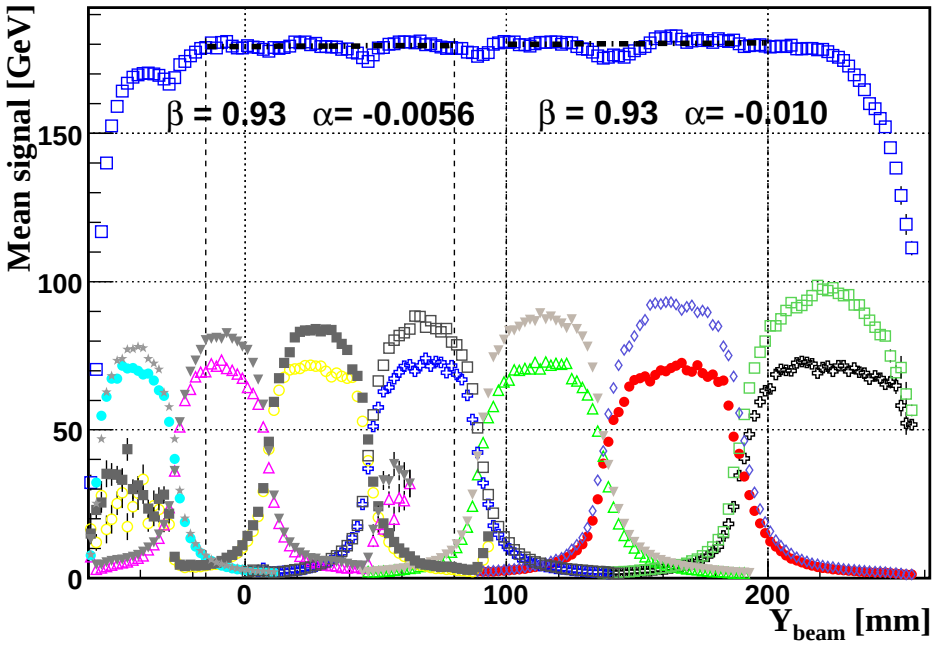

Fig. 11. Vertical (i.e.η) scan with electrons of 193 GeV defined by a EMEC cone size of $R = 0.15$. Shown is the response after correction for the η dependence for the total cone energy. To crosscheck the correction, the fit has been repeated and the fitted parameter α is indeed compatible with 0 within errors. The parameter β is somewhat smaller than 1 - as would be expected - due to the smaller cone size ($R = 0.15$ rather than $R = 0.25$) used. In addition at each impact point all individual cell signals above 5% of the total signal are shown.

5.1.2 Linearity and Energy Resolution

The response as function of energy has been studied for electrons in the EMEC region using a cone size of $R = 0.15$ and $R = 0.25$ as mentioned above. To obtain the electromagnetic scale (see section 3.2) the data have been normalized to the beam energy at 119 GeV for the cone size $R = 0.25$ and the average of the impact points D and E. Thus any contribution due to noise is minimized and the normalization not restricted just to one impact point. But any leakage of the electron signal outside the cone is for $R = 0.25$ negligible. Because of the finite size of the cone, the energy depends on the exact impact point in η and ϕ. The residual η correction takes the signal variation with η within a given cell into account, as expected from the electric field variation with η. In addition, with respect to ϕ, this effect is convoluted with sampling variations due to the ϕ-modulation of the EMEC absorbers. In a first step these corrections have not yet been taken into account (for details see following text for 3x3 and 5x5 cell reconstruction). Fig. 12 shows the response as function of energy for these electromagnetic clusters for the EMEC impact point D (corresponding to $|\eta| = 2.8$, see Fig. 8). The size of the cone is $R = 0.15$ or

$R = 0.25$. The expectations from MC simulation are shown as well. For the cone size of $R = 0.15$ the leakage out of cluster is $\sim 4\%$ at high energies. The linearity is well described by the MC, the deviations at low energies are to a large extent due to the dead material in the beam in front of the active EMEC calorimeter, as expected from and seen in MC simulations.

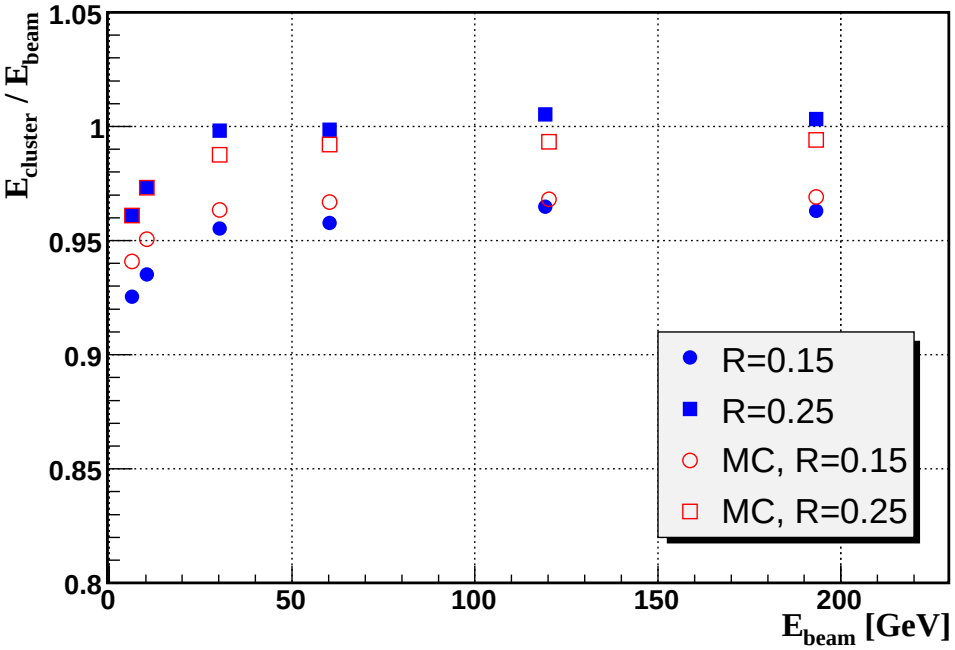

Fig. 12. Energy dependence of the response to electrons with the impact point in EMEC. Shown are the results for a cone size $R = 0.15$ and $R = 0.25$. The expectations from MC simulations are shown as well.

Similarly the energy resolution has been studied for electrons reconstructed in a cone as defined above. The results are shown in Fig. 13 after noise subtraction and compared with MC expectations. The resolution has been parameterized using

$$\frac{\sigma(E)}{E} = \frac{a}{\sqrt{E}} \oplus b. \tag{2}$$

For the larger cone option the data yield typically a sampling term of $a = (13.5 \pm 0.5)\,\%\sqrt{\mathrm{GeV}}$ and a constant term $b = (0.7 \pm 0.1)\,\%$. In general, the energy resolution expected from MC is somewhat better than seen in the data. This holds for both cone sizes, particularly at low energies. For the larger cone option the MC prediction is approaching the data at higher energies. But for the smaller cone option the data yield a somewhat larger constant term. To allow comparison with previous beam test results an electron reconstruction using fixed size clusters based on 3x3 and 5x5 cells has been used. Here also

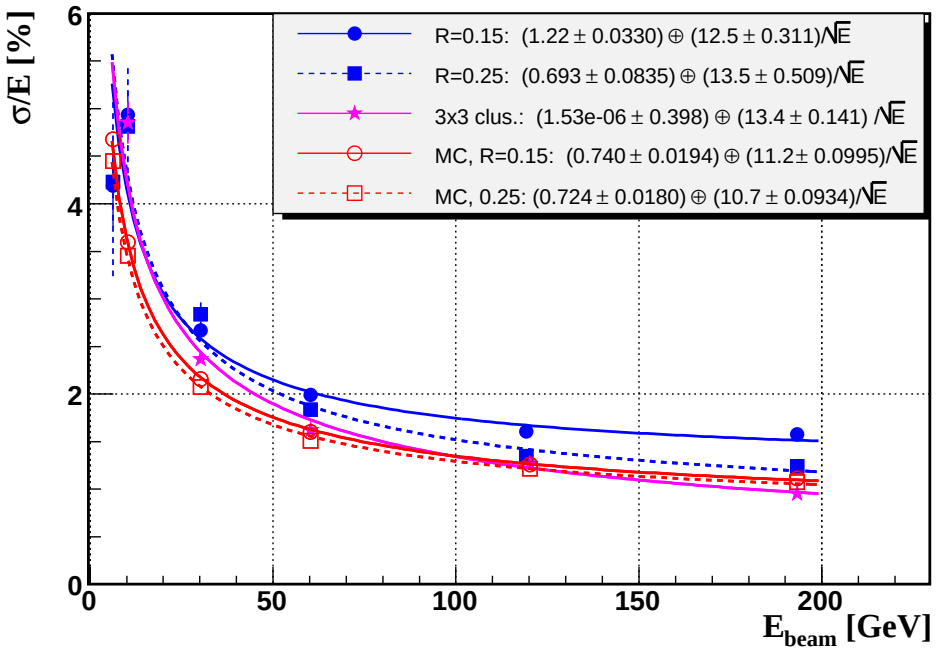

Fig. 13. Energy dependence of the energy resolution for electrons with the impact point in EMEC. Shown are the results for a cone size of $R = 0.15$ and $R = 0.25$. The expectations from MC simulations are shown as well. Also shown are the results for the 3x3 cluster reconstruction where all higher level corrections are included.

further higher level corrections have been applied (for details see [4]). After correction for the high voltage effect, there is still a residual η modulation to be corrected. This correction arises from the finite cluster size, and also from residual local high voltage effects due to the complicated geometry of the detector. If the modulation were only due to finite cluster size effects, the η modulation would be well fitted by a parabola. This is not the case here, and the correction has been computed cell by cell by a third-degree polynomial. This correction amounts up to 2% locally. After correction of the η modulation, the ϕ modulation due to the periodic structure of the absorbers has to be corrected. This correction has also been fitted η cell by η cell, using a Fourier development of the reponse as a function of ϕ. The effect of the ϕ modulation is smaller than the η modulation, amounting to less than 1%. After η and ϕ corrections have been applied, the dispersion of the calorimeter response has been evaluated over 16 beam impact points in η, positioned at the same ϕ. This dispersion has been found to be 0.3%. In addition, it has been checked that the response between different ϕ positions did not differ by more than 1%. These results ensure that the uniformity of the module is better than 1%. The results are in good agreement with previous measurements [1,4].

Fig. 14 shows the response as function of energy for these two modes (3x3 and 5x5) of cluster reconstruction. The electromagnetic scale has been obtained by

normalizing the reconstructed energy to the beam energy averaging over the high energy data and many different beam impact points. As out-of-cluster leakage corrections are covered (see above), in both cases the linearity is very good, except for the low energy where energy losses due to inactive material in front of the calorimeter have to be taken into account. The energy response for the larger cone with $R = 0.25$ is rather similar. But applying a 3 σ noise cut in addition yields obviously larger signal losses at low energies.

Finally the topological cluster reconstruction, based on geometrical information of neighbouring cells has also been used. For electron reconstruction an optimized parameter set used frequently is 6/3/3 (σ) [22]. This set is typical for the reconstruction of high energy electrons, cutting into the signal at the perimeter of the cluster with 3σ. As we are dealing here with the electron reconstruction in the forward region of ATLAS, the main emphasis is on the reconstruction of high energy particles. Fig. 14 also shows the response as function of energy for the 6/3/3 cluster reconstruction. The normalization used is as discussed above for the cone of $R = 0.25$. The noise suppression is rather effective and close to that obtained in the cone reconstruction using the 3 σ noise cut. At energies below 100 GeVsignal losses are increasing. Nevertheless, the energy resolution is for this case better than for the option with e. g. lower σ cuts. The energy dependence of the energy resolution using the topological cluster reconstruction has been studied as well. The results are shown in Fig. 15. Here the topological cluster reconstruction is compared with other techniques, the noise is not subtracted. The 3x3 cluster method, which includes all higher level corrections, yields the best results. The topological cluster reconstruction as well as the cone reconstruction with 3 σ noise cuts in addition are only slightly worse. This holds also for a signal reconstruction based on a cone of $R = 0.17$, which for the cone method gives the best results when comparing with $R = 0.15$ or $R = 0.25$. The lines show the result of a fit using the ansatz

$$\frac{\sigma(E)}{E} = \frac{a}{\sqrt{E}} \oplus b \oplus \frac{c}{E}. \tag{3}$$

i.e. taking the noise contribution (in GeV) via the term c explicitly into account. But as the noise is not constant (see chapter 3.3), which yields also a variation with energy, the fit is meant just to guide the eye rather than for the extraction of the specific energy resolution parameters.

For the 3x3 cluster method the noise has been subtracted at each energy point similarly to the cone approach. The results for the energy dependence of the energy resolution are shown in Fig. 13 as well. The resolution has been again parameterized using equation (2). The data yield typically a sampling term of $a = (13.4 \pm 0.1)\,\%\sqrt{\mathrm{GeV}}$ and a constant term $b = (0.0 \pm 0.4)\,\%$. In the 3x3 cluster method the higher level corrections are taken into account. Evidently

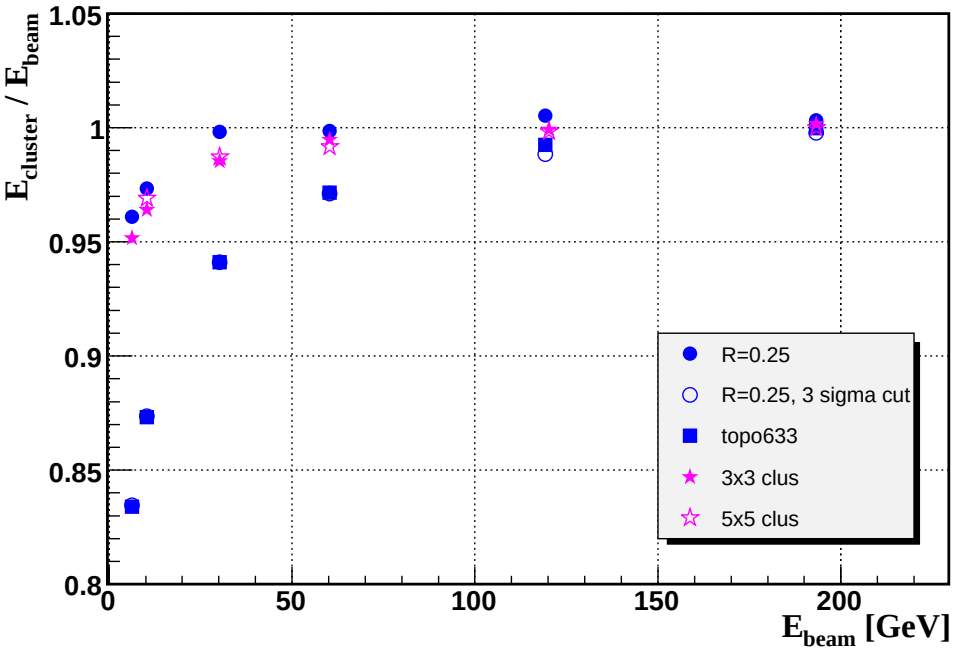

Fig. 14. Energy dependence of the response to electrons with the impact point in EMEC. Shown are the results for clusters of fixed size 3x3 and 5x5 cells where all higher level corrections have been added. For comparison are shown also the results of cone size $R = 0.25$ (see above) and applying a 3 σ noise cut in addition. The results for topological cluster reconstruction (6/3/3) are shown as well.

this yields the best energy resolution at high energies, where these corrections start to get visible. At lower energies the resolution is similar to the cone approach, where these corrections are ignored. The results are in agreement with previous measurements [1,4].

5.2 Electrons in FCal Region

5.2.1 Linearity and Energy Resolution

The response as function of energy has been studied for electrons in the FCal (impact point H) in a very similar way as in the EMEC. Again two different cone sizes have been chosen to reconstruct the energy: $R = 0.15$ and $R = 0.25$. Fig. 16 shows the results for the data (full symbols) as well as MC expectations (open symbols). For the normalization the response at the highest energy and for the cone size $R = 0.25$ has been normalized to the beam energy. Again, the energy losses at low energy are due to the additional inactive material present in front of the active calorimeter as known from MC studies. The MC simulation predicts, in particular for low energies, a somewhat larger cluster response than seen in the data. But the deviations are rather small. The

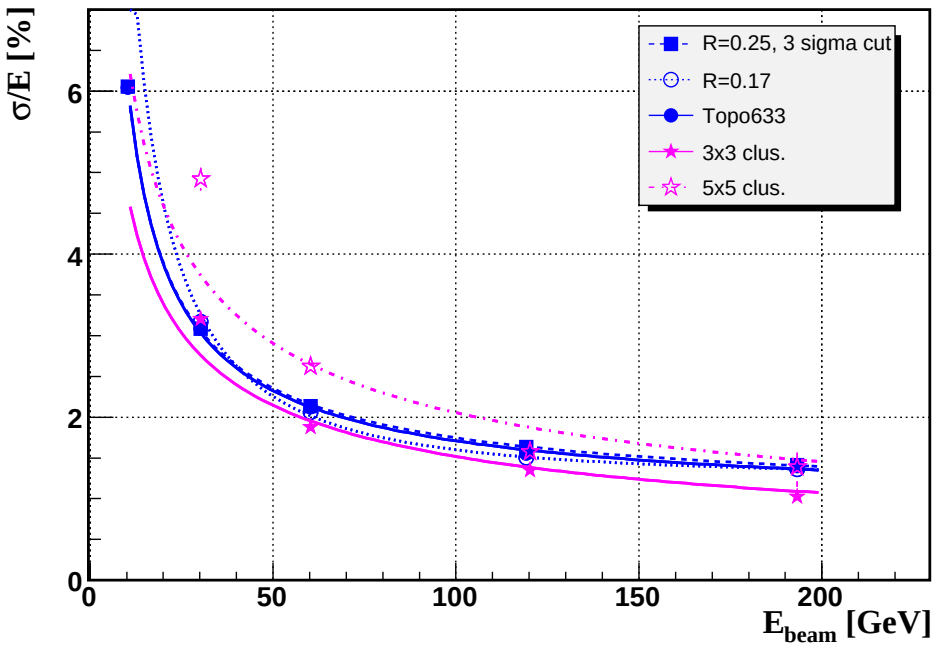

Fig. 15. Energy dependence of the energy resolution for electrons with the impact point in EMEC without noise subtraction. Shown are the results for clusters of fixed size 3x3 and 5x5 cells where all higher level corrections have been added. For comparison are shown also the results of cone size $R = 0.25$ (see above) and applying a 3 σ noise cut in addition. The results for topological cluster reconstruction (6/3/3) are shown as well. The fit (lines) is meant just to guide the eye.

leakage for the cone size of $R = 0.15$ is ~ 5 % at high energies.

The related energy resolution as function of energy and after noise subtraction is shown in Fig. 17. The resolution has again been parameterized using equation (2). For the larger cluster size the data yield a sampling term of $a = (29.3 \pm 0.7)\,\%\sqrt{\mathrm{GeV}}$ and a constant term $b = (3.0 \pm 0.1)\,\%$. Reducing the cluster to $R = 0.15$ increases the constant term slightly from 3.0% to 3.2%. The MC expectation yields a noticeable worse resolution, giving a constant term of 3.8 ± 0.1 % and a sampling term of $a = (30.7 \pm 0.3)\,\%\sqrt{\mathrm{GeV}}$ for the larger cluster option. The results are comparable with previous measurements [8].

Alternatively the topological cluster reconstruction (see above) has been also used. Again, for electron reconstruction the parameter set 6/3/3 (σ) has been chosen as used frequently in previous MC studies [22]. Fig. 18 shows the response as function of energy for the 6/3/3 cluster reconstruction. For comparison also the cone method ($R = 0.25$) and the cone method adding a simple 3 σ noise cut are shown. Clearly the topological cluster reconstruction reduces the response at low energies. In general the topological cluster reconstruction

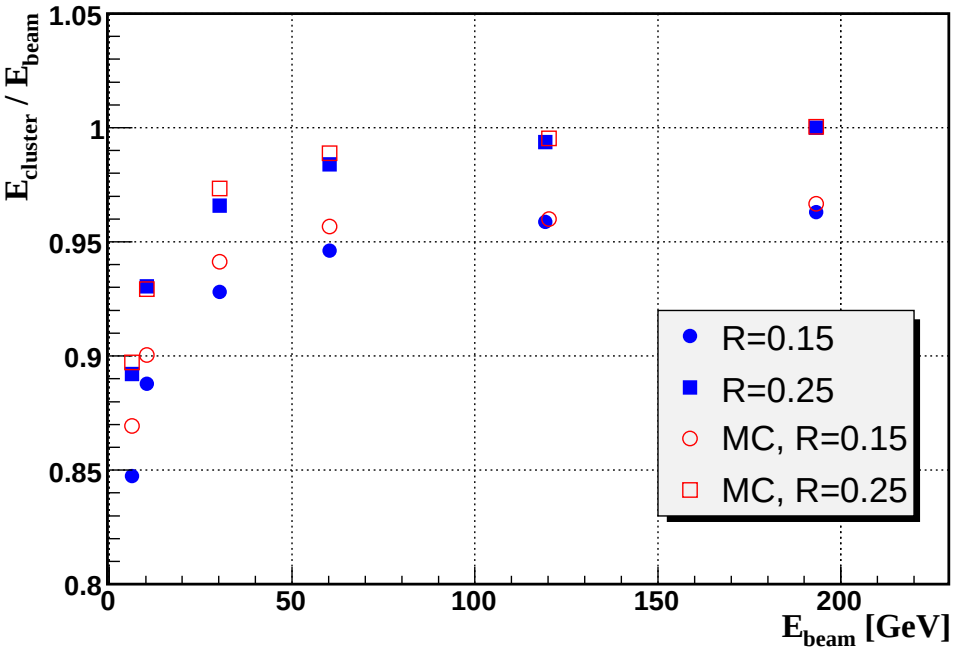

Fig. 16. Energy dependence of the response for electrons with the impact point in FCal. Shown are the results for a cone size of $R = 0.15$ and $R = 0.25$. The expectations from MC simulations are shown as well (open points).

follows closely the response using the cone approach with the additional 3 σ noise cut. Only at very low energies the reduction of the signal is substantially less than in the cone approach with the additional 3 σ noise cut (for $E < 10$ GeV below scale). The advantage of the topological cluster reconstruction is obviously the noise reduction without reducing the response too strongly.

Finally the energy dependence of the energy resolution has been analyzed for the topological cluster reconstruction in comparison with the cone approach ($R = 0.25$) or cone approach adding a 3 σ noise cut. Again, the noise has not been subtracted (see EMEC results above). The results are shown in Fig. 19. Again, the lines show the result of a fit using the equation (3), i.e. taking the noise contribution explicitly into account. The fit is meant just to guide the eye (see above). The three methods yield rather similar results.

5.3 Vertical Scan with Electrons

Detailed vertical scans with electrons reveal the fine structure of the transition from the EMEC/HEC region to the FCal region. Details of the related energy corrections for the losses due to the dead material will be discussed in a forthcoming paper. Here the main issue is a cross-check of the alignment

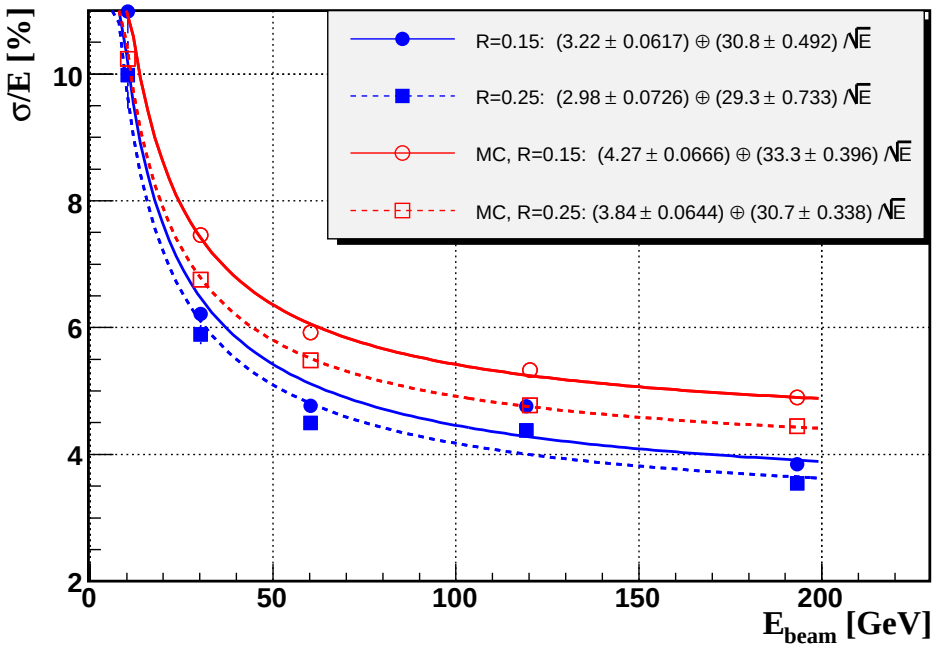

Fig. 17. Energy dependence of the energy resolution for electrons with the impact point in FCal. Shown are the results for a cone size of $R = 0.15$ and $R = 0.25$. The expectations from MC simulations are shown as well (open points).

of the various support structures, LAr excluders and FCal support tube and forward cone by comparing the data with MC simulation. As the simulation of electromagnetic showers are known to be very close to reality, any deviations from the data could point to shortcomings in the description of the dead material present. For pions the acceptance of the set-up is rather limited, therefore any leakage effects or losses due to dead material need to be understood prior to drawing conclusions about the quality of the hadronic simulation. Here the correct geometrical description of the set-up is of utmost importance (see vertical scan with pions, chapter 6.2). In addition, scans over larger areas yield vital information on the homogeneity of the signal response within the given acceptance.

Fig. 20 shows the response for electrons of 193 GeV when performing a vertical scan at $x = 0$ covering almost the full acceptance. A cone size of $R = 0.15$ has been used. The energy normalization has been done as described in section 5.1.2 for the EMEC and 5.2.1 for the FCal. Shown is the total response as well as the response in the main longitudinal section of either the EMEC or FCal. The data are compared with MC expectations using GEANT 4 QGSP-GN 2.6. The acceptance edges of the FCal and EMEC are well reproduced by the MC simulation. This holds also for the transition region, although smaller deviations in the crack region are visible. The small deviation of the data from MC prediction at $y \sim -115\,mm$ is due to a weak response of a single electronic

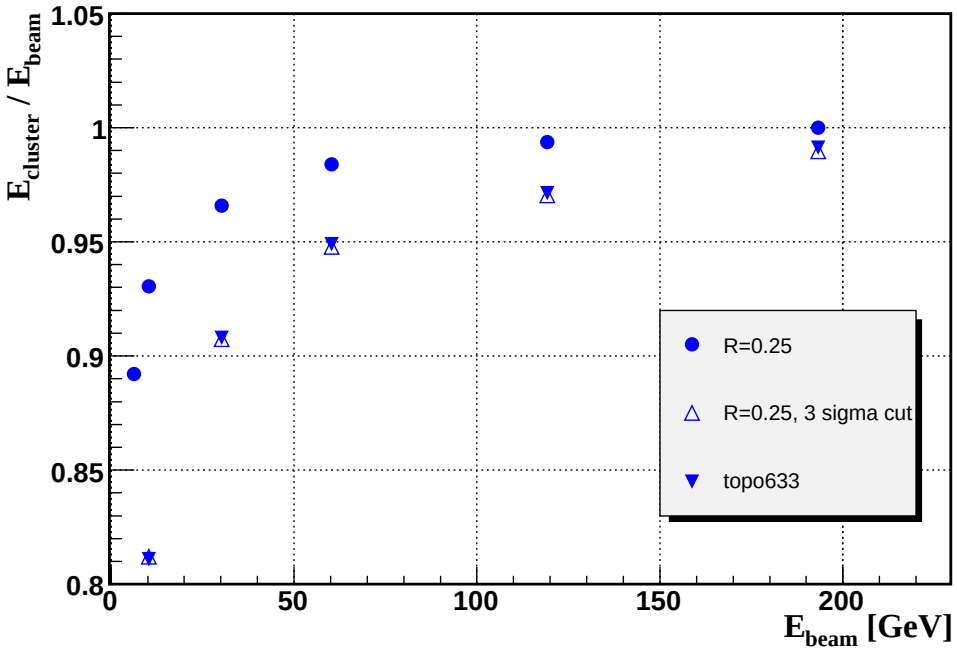

Fig. 18. Energy dependence of the response to electrons with the impact point in FCal. Shown are the results for the topological cluster reconstruction (6/3/3) in comparison to the cone approach with a cone size of $R = 0.25$. Also shown is the result when adding a 3 σ noise cut for the cone reconstruction (for $E < 10$ GeV below scale).

channel in the data. The first drop of the signal close to $y \sim -95$ mm is due to the cold wall in front of the FCAL1 centered at $|\eta| \simeq 3.2$ (for comparison see Fig. 1). The second drop of the signal at $y \sim -60$ mm is finally the cross over of the acceptance boundaries of FCAL1 and EMEC.

5.4 Discussion of Electron Results

The first choice for the reconstruction of isolated electrons and photons in ATLAS will be based on the fixed size cluster reconstruction using 3x3 or 5x5 cells. An alternative is also in this case the topo cluster reconstruction, which yields similar results. The jet reconstruction and hadronic calibration in ATLAS employs the topo cluster reconstruction as the essential first step. The important issues are here the optimal signal reconstruction in presence of noise and pile-up, the identification of electromagnetic clusters in the first step, and finally the weighting scheme to compensate for the different response of electrons and hadrons in the ATLAS calorimeter. The validation of the full hadronic calibration in beam tests will be discussed in a forthcoming paper.

In the forward region of ATLAS, studied in this beam test, the electron en-

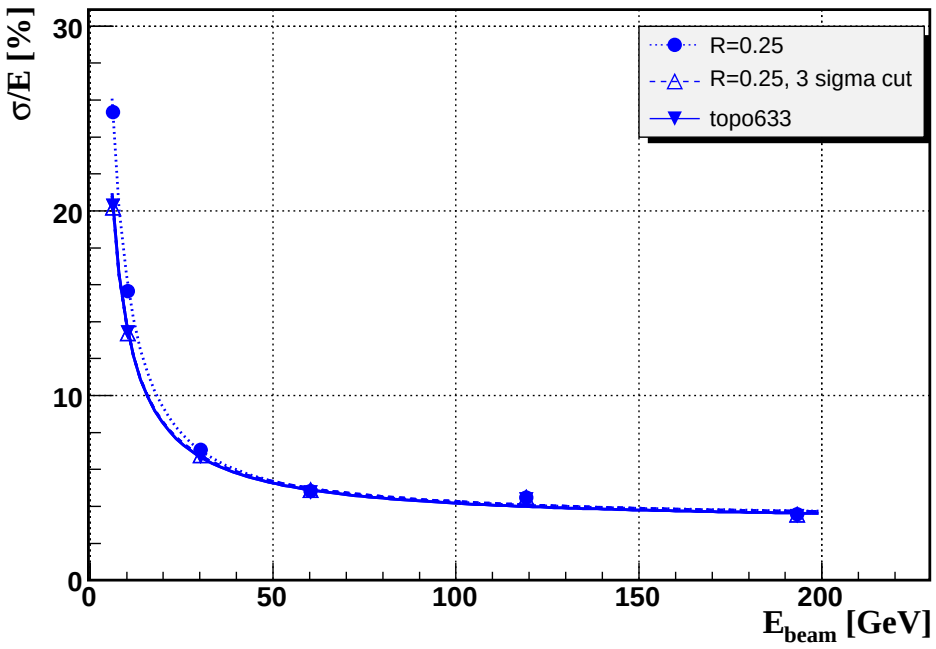

Fig. 19. Energy dependence of the energy resolution for electrons with the impact point in FCal (without noise subtraction). Shown are the results for the topological cluster reconstruction (6/3/3) in comparison to the cone approach with a cone size of $R = 0.25$. Also shown is the result when adding a 3 σ noise cut for the cone reconstruction. The fit (lines) is meant just to guide the eye.

ergies are rather high. Also the pile-up and general noise are - in comparison to the central region - substantially higher. Therefore the topo cluster reconstruction parameters chosen should be effective in the supression of this background, but on the other hand signal losses at low energies have to be taken into account. The EMEC as well FCal data show that for energies above 100 GeV these signal losses are minimal. In addition, the energy resolution is very close to the ideal situation when any noise contributions are ignored.

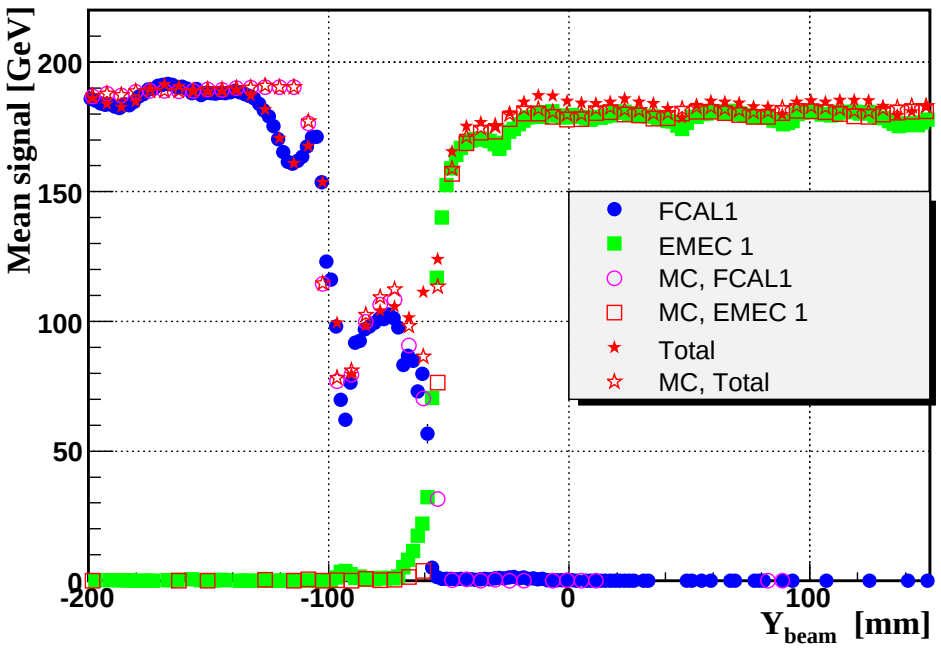

Fig. 20. Energy response for electrons of 193 GeV when performing a vertical scan covering almost the full acceptance. Shown is the total response as well as the response in the main longitudinal section of either the EMEC or FCal. The data are compared with MC expectations.

6.1 MC Expectations for Pions in ATLAS on Electromagnetic Scale

Previous studies in beamtests have been carried out at lower $|\eta|$ values, e.g. at $1.6 < |\eta| < 1.8$ (see [6],[9]). This beamtest has been done for a higher $|\eta|$ region. The effect of the 'crack' region at $|\eta| = 3.2$ starts to be visible for pions already when approaching this region. Fig. 21 shows the MC prediction (GEANT 4 QGSP-GN 2.6) for the variation in response (at the electromagnetic scale) with $|\eta|$ for 200 GeV pions. Shown are the expectations for two different cone sizes R in $\Delta\eta \times \Delta\phi$. The impact point D, used to study the EMEC/HEC region, corresponds to an impact point in ATLAS of $|\eta| = 2.8$. The local variations are partially due to the fine structure of the calorimeter (tie rods etc.). Beyond $|\eta| = 2.7$ the response starts to drop due to energy losses in the dead material. In consequence, the energy resolution is affected as well. Fig. 22 shows the MC prediction of the variation of the energy resolution $\frac{\sigma(E)}{E}$ of 200 GeV pions with $|\eta|$. Again, beyond $|\eta| = 2.7$ the resolution starts to worsen from typically $\frac{\sigma(E)}{E} = 8\%$ to $\frac{\sigma(E)}{E} = 10\%$ at $|\eta| = 2.8$ (point D) and to $\frac{\sigma(E)}{E} = 15\%$ at $|\eta| = 3.0$.

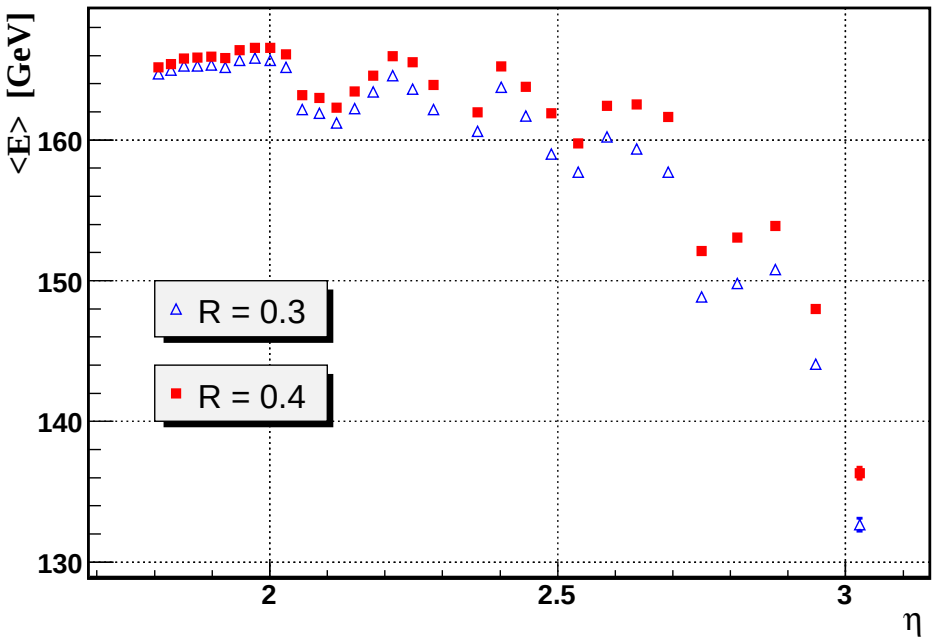

Fig. 21. Response to 200 GeV pions in ATLAS on the electromagnetic scale. Shown is the variation of the MC expectation with $|\eta|$ for cone sizes of $R = 0.3$ and $R = 0.4$.

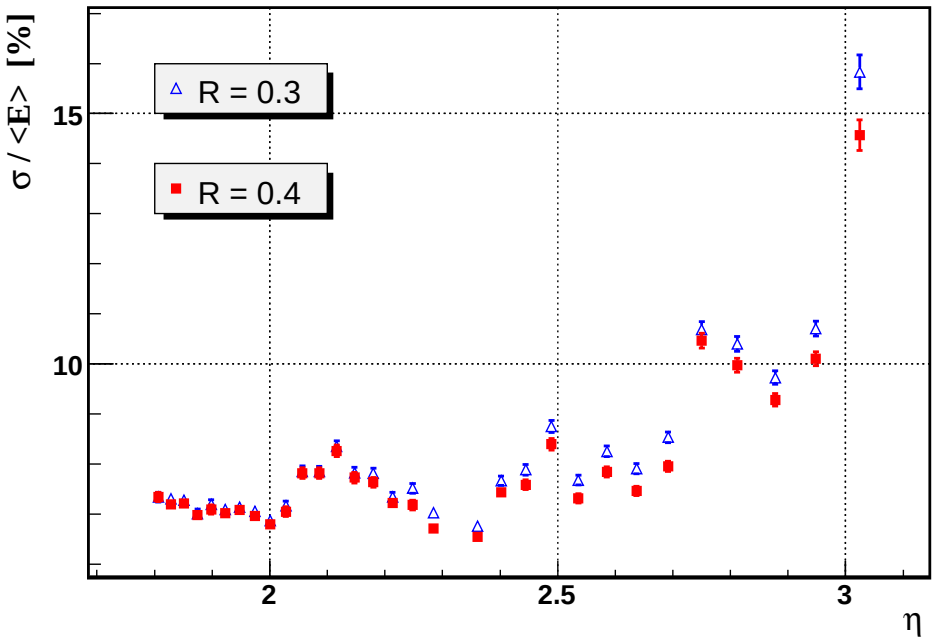

Fig. 22. Energy resolution of 200 GeV pions in ATLAS on electromagnetic scale. Shown is the variation of the MC expectation with $|\eta|$ for a cone size of $R = 0.3$ and $R = 0.4$.

6.2 Vertical Scan with Pions

As was the case for electrons, a vertical scan of the response to pions can reveal the fine structure of the hadronic calorimeters of the set-up. But in contrast to electrons, here both the electromagnetic scale as well as the hadronic shower size (longitudinal and transverse) are subject to larger uncertainties in simulations. On the other hand any deviations of the data from MC expectations in this set-up with different absorber materials and rapidly changing transitions, can give important feed-back to MC simulation parameters and algorithms. Figs. 23 and 24 show the response on the electromagnetic scale for pions of 200 GeV. Shown are the data (full symbols) as well as the expectations from MC (open symbols, GEANT 4 QGSP-GN 2.6). This vertical scan has been done at a horizontal position of $x = -60$ mm to avoid the small intermodule gap of the HEC at $x = 0$ mm. Fig. 23 shows the response in the different longitudinal sections of the EMEC (EMEC1 and EMEC2) as well as the total response in the electromagnetic sections FCAL1 and EMEC. Fig. 24 shows the corresponding results for the longitudinal sections in the HEC (HEC1, HEC2 and HEC3) as well as the total response in the hadronic sections FCAL2 and HEC. For the pion energy reconstruction a cone size of $R = 0.30$ has been used. Larger cone sizes would start to enhance acceptance boundary effects in comparison to the direct energy losses in the crack region. Because the main

focus is here on a cross check of the correct geometry in MC simulation, the smaller cone size follows somewhat closer the material variation in the crack region. On the other hand the cone size of $R = 0.30$ is large enough to collect a substantial part of the total pion response and thus enables a precise comparison of the data with MC simulation.

In general, the MC predicts a larger signal in the electromagnetic sections and a smaller one in the hadronic sections compared to the data. This is a well known problem in the GEANT 4 QGSP and QGSP-GN simulations, yielding somewhat more compact hadronic showers than seen in the data. Except for this overall scale factor, the MC shows a rather good agreement with the data, in particular for the details of the response when passing the crack region. The variation of the HEC response at $y \sim 140$ mm is due to the HEC tierods.

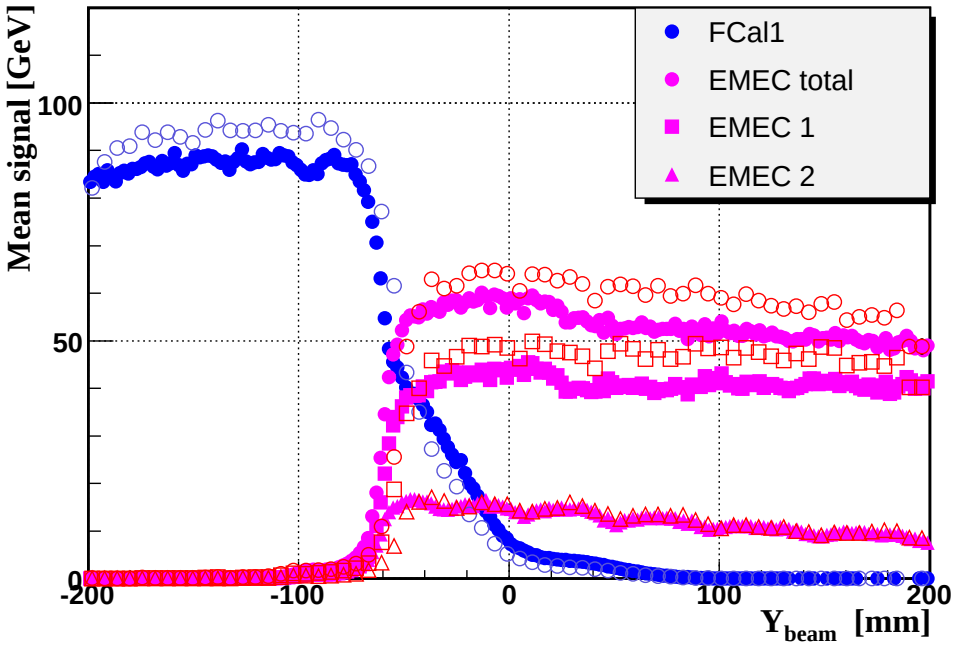

Fig. 23. Energy response on the electromagnetic scale for pions of 200 GeV when performing a vertical scan covering almost the full acceptance. Shown is the response in the total electromagnetic part, FCAL1 and EMEC, as well as in the two main longitudinal sections of the EMEC. The data (full symbols) are compared with MC expectations (open symbols, GEANT 4 QGSP-GN). For the energy reconstruction a cone size of $R = 0.30$ has been used.

Finally Fig. 25 shows the total signal as well as the total response in the related electromagnetic and hadronic sections of the calorimeter. Again, for the energy reconstruction a cone size of $R = 0.30$ has been used. The total response in the EMEC/HEC and FCAL region is typically 145 GeV on electromagnetic scale, yielding an effective e/π ratio for this combined set-up of about 1.38.

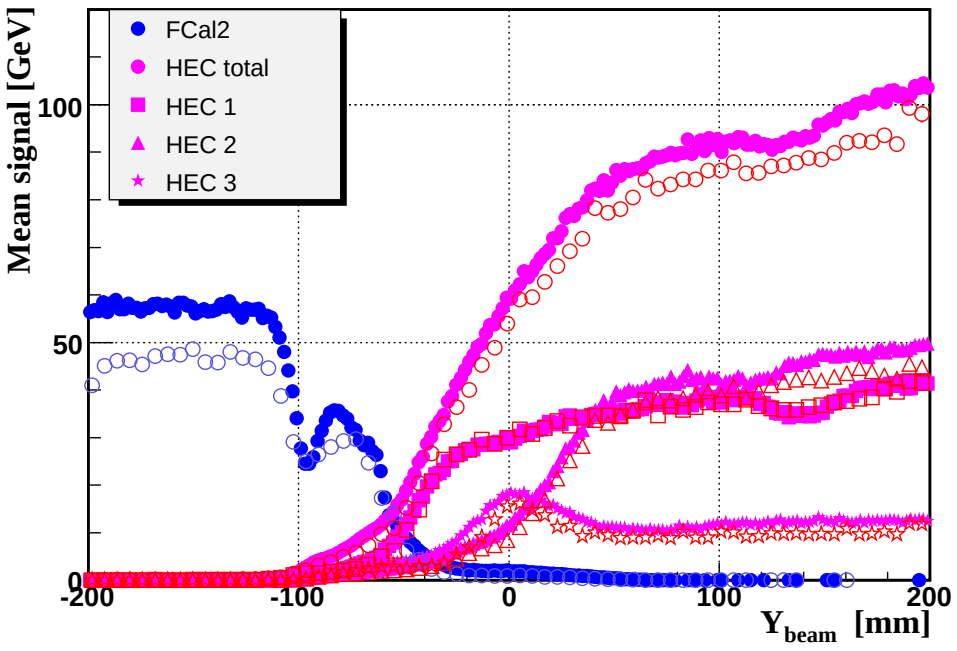

Fig. 24. Energy response on the electromagnetic scale for pions of 200 *GeV* when performing a vertical scan covering almost the full acceptance. Shown is the response in the total hadronic part, FCAL2 and HEC, as well as in the individual longitudinal sections of the HEC (HEC1, HEC2, HEC3). The data (full symbols) are compared with MC expectations (open symbols, GEANT 4 QGSP-GN). For the energy reconstruction a cone size of $R = 0.30$ has been used.

The signal losses in the crack are typically at the level of 20%.

In general, the response on the electromagnetic scale for 200 GeV pions is reproduced by the MC simulation reasonably well, but with some deviations when comparing details in the longitudinal structure. Partially this could be explained by a too compact hadronic shower size in the MC, a well known effect observed also in earlier beam tests (see e.g. [18]).

6.3 Pions in EMEC/HEC Region

6.3.1 Response on Electromagnetic Scale

The response as function of energy has been studied for pions in the EMEC/HEC region using energy deposits on electromagnetic scale within a cone of $R = 0.3$ and $R = 0.5$. Fig. 26 shows the response as function of energy for the impact point D (corresponding to $|\eta| = 2.8$). The expectations from MC simulations are shown as well. The data for the smaller cone size are somewhat below the MC expectations (open points), in particular at low ener-

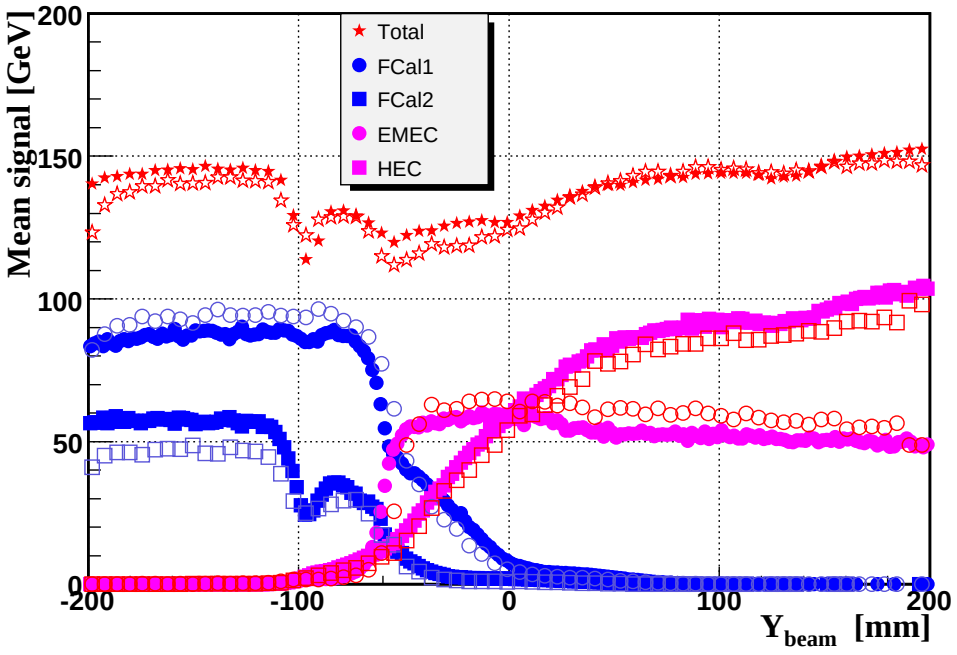

Fig. 25. Energy response on the electromagnetic scale for pions of 200 *GeV* when performing a vertical scan covering almost the full acceptance. Shown is the total signal as well as the related response in the total electromagnetic and hadronic sections of the calorimeter. The data (full symbols) are compared with MC expectations (open symbols, GEANT 4 QGSP-GN). For the energy reconstruction a cone size of $R = 0.30$ has been used.

gies. For the larger cone size the effect is reduced. Part of the difference might be the rather compact lateral shower size in GEANT 4 QGSP with respect to the data, an effect which seems to be more pronounced at low energies (see e.g. [18]). For the larger cone size the MC describes the data reasonably well at higher energies. The topological cluster reconstruction for pions has been compared with the cone method. For pion reconstruction an optimized parameter set used frequently is 4/2/0 (σ). Fig. 27 shows the response as function of energy for the 4/2/0 cluster reconstruction. The response is somewhat less than for the cone approach ($R = 0.5$), but larger than using the cone approach in combination with a simple 2 σ noise suppression. This is expected, as in the 4/2/0 cluster reconstruction perimeter cells are kept without any additional σ noise suppression.

6.3.2 Energy Resolution using the 'Bench Mark' Approach

The energy resolution for pions is affected by the different and in addition energy dependent response to pions in the different calorimeter sections, mainly due to the different absorber materials in use. Thus any difference in longitudinal shower shape between data and MC will immediately lead to a difference

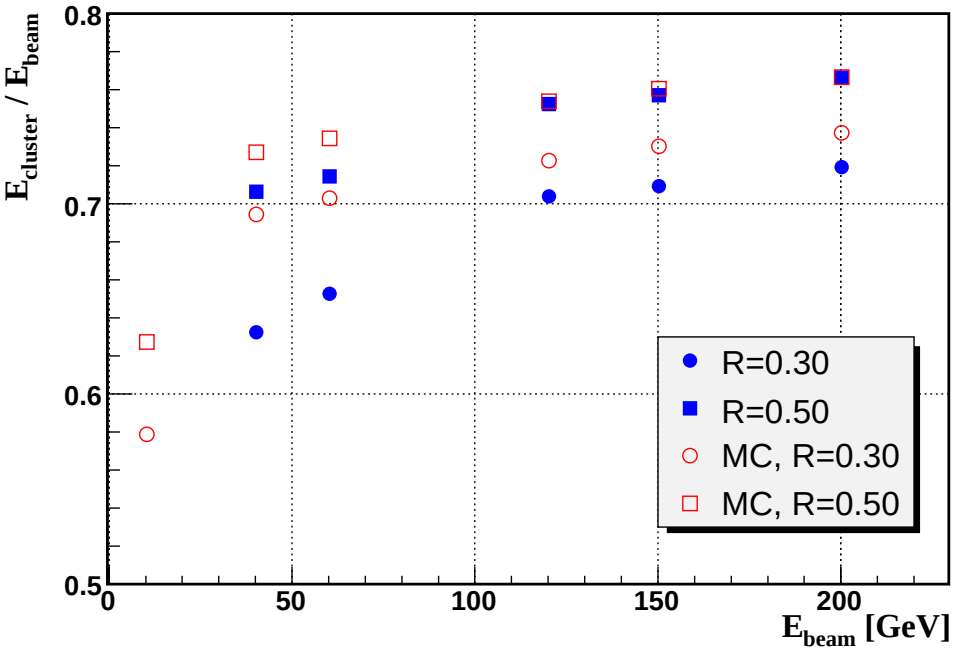

Fig. 26. Energy dependence of the response to pions with the impact point in EMEC using the electromagnetic scale. The energy has been reconstructed within a cone of $R = 0.3$ and $R = 0.5$ respectively. The expectations from MC simulations (open points) are shown as well.

in resolution. This effect would be even more pronounced when energy leakage needs to be taken into account due to the limited acceptance. Therefore we tried to compare the data with MC simulations using the 'bench mark approach', where one calibration constant per longitudinal section and energy is used, rather than one overall calibration constant at each energy as done in the HEC stand alone beam tests (for details see [6]). This calibration constant has been obtained by minimizing the energy resolution for each energy point. Again, for the energy reconstruction a cone of $R = 0.3$ and $R = 0.5$ has been assumed. For the EMEC sections these calibration constants are rather energy independent. For the HEC1 and HEC2 sections they follow the weak energy dependence of the e/π ratio in HEC. The HEC3 section is in addition sensitive to longitudinal energy leakage and this is reflected in a slowly rising calibration constant with energy. Fig. 28 shows the energy resolution as function of energy for the impact point D. The expectations from MC simulations (open points) are shown as well. The noise has been subtracted. The energy resolution expected from the MC simulation (GEANT 4 QGSP-BERTINI) is in rather good agreement for the higher energies and for the larger cone, but at low energies is somewhat better than what is seen in the data. The resolution has been parameterized using equation (2). The data for the cone size $R = 0.5$ yield typically a sampling term of $a = (88 \pm 5)\,\%\sqrt{\mathrm{GeV}}$ and a constant term $b = (6.8 \pm 0.4)\,\%$ whereas the MC expectations are $a = (72 \pm 1)\,\%\sqrt{\mathrm{GeV}}$

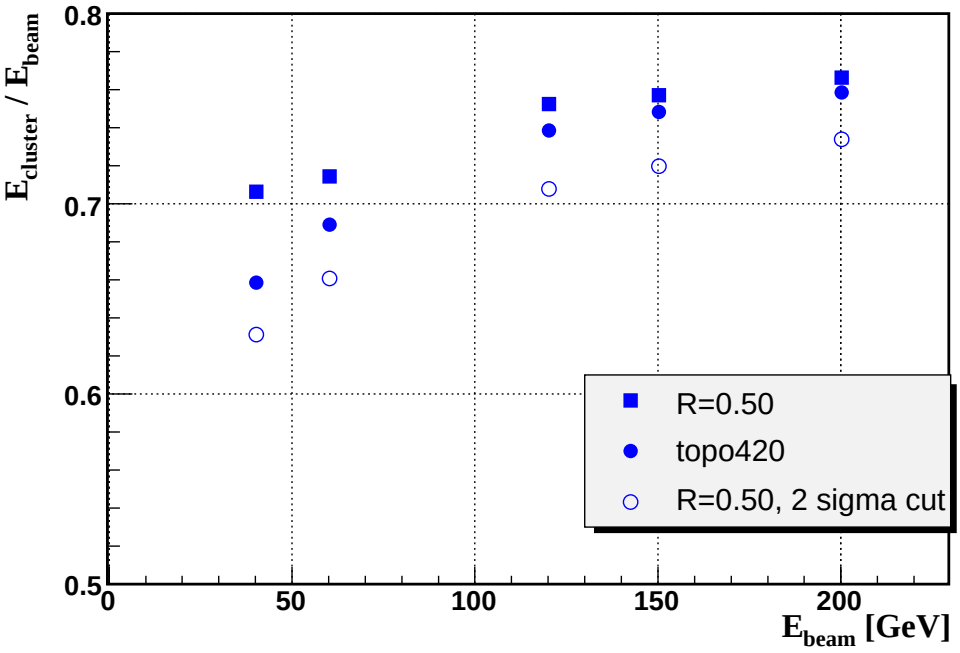

Fig. 27. Energy dependence of the response to pions with the impact point in EMEC using the electromagnetic scale. The energy has been reconstructed using the topological cluster reconstruction (4/2/0 σ) and compared with a cone reconstruction ($R = 0.5$). For comparison also the cone reconstruction with an additional 2 σ noise suppression cut is shown as well.

and $b = (7.5 \pm 0.1)\,\%$ respectively. The differences in the terms obtained are largely driven by the somewhat different energy dependence, yielding a better resolution for the MC at low energies, but being in agreement with the data at high energies. Finally the energy dependence of the energy resolution using the topological cluster reconstruction has also been studied. The noise has been not subtracted for these studies. Fig. 29 compares the result for the topological cluster reconstruction with the cone reconstruction ($R = 0.5$) with and without the application of a 2 σ noise cut. Again, the fit to equation (3) using the sampling, constant and noise term, is meant just to guide the eye rather than extract the specific energy resolution parameters. The topological cluster reconstruction yields an optimal energy resolution for almost the whole energy range, except for the very low energies. Here it is slightly worse than the cone approach with the simple noise suppression (2 σ cut) added.

6.3.3 Longitudinal Shower Shape

The longitudinal shower shape has been studied for pions with the impact point in EMEC. The cluster energy, using the electromagnetic scale, has been reconstructed within a cone of $R = 0.5$ for the various energies. Fig. 30 shows

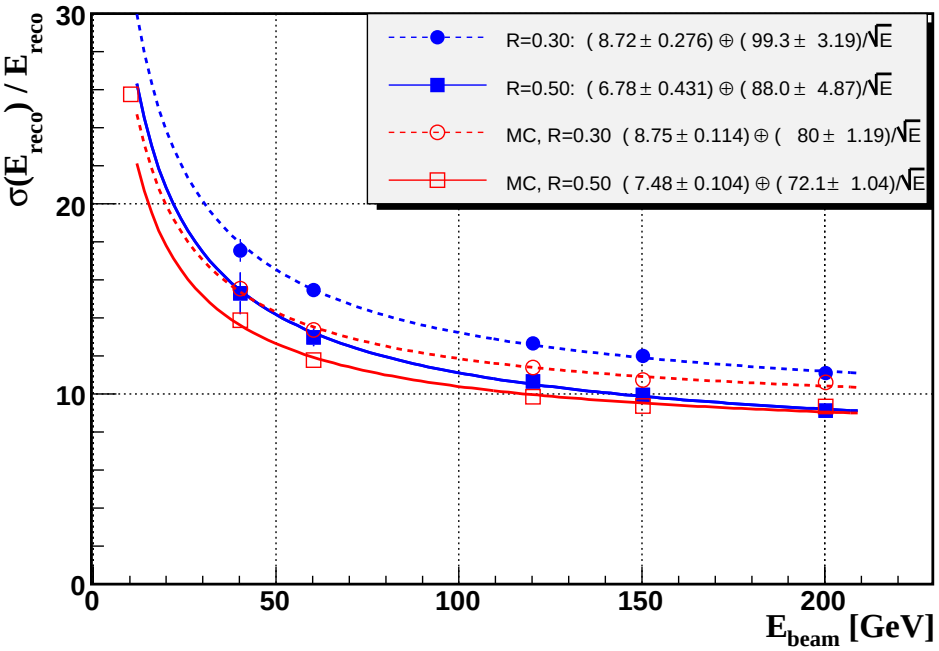

Fig. 28. Energy dependence of the energy resolution for pions with the impact point in EMEC using the bench mark approach. Here one calibration constant per longitudinal section has been determined from a fit minimizing the energy resolution. The energy has been reconstructed within a cone of $R = 0.3$ resp. $R = 0.5$. The expectations from MC simulations (open points) are shown as well.

the comparison of the data (full symbols) with the MC prediction (open symbols) using GEANT 4 with the QGSP-BERTINI (QGSP-GN yields rather similar results) physics list. In general the MC prediction is close to the data, except for some larger energy deposits in the main longitudinal EMEC section (EMEC1) and slightly smaller energy deposits in HEC 1 and HEC 2. This might be again a hint of the too compact shower size in GEANT 4 QGSP with respect to the data.

6.3.4 Lateral Shower Shape

The lateral shower shape has been studied using a horizontal scan with pions at 60 GeV (see Fig. 31). Shown is the energy in individual ϕ wedges of $\Delta\phi = 0.2$, integrated in η and summed for the EMEC and HEC calorimeters. At each pion impact point the eight contributing signals (8 ϕ wedges) using the electromagnetic scale have been studied, two of them are rather small. The six most relevant signals are shown for the data (solid points) and MC prediction (open points) using GEANT 4 with the QGSP-BERTINI physics list. The symmetry between left and right signal response is slightly violated because one channel with a weak response close to $x = 40$ mm lowers the response

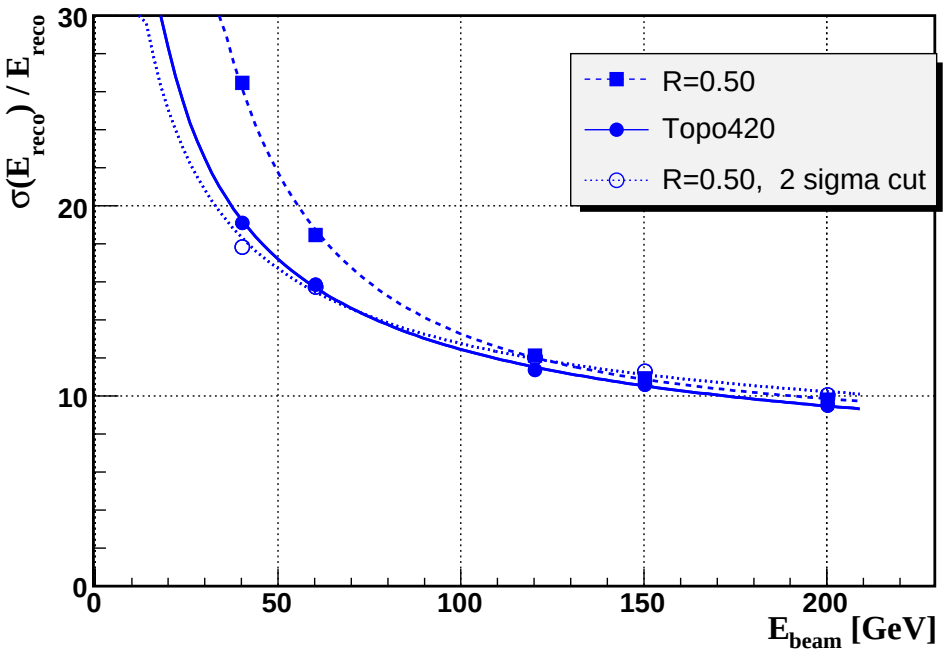

Fig. 29. Energy dependence of the energy resolution for pions with the impact point in EMEC using the bench mark approach. Here one calibration constant per longitudinal section has been determined from a fit minimizing the energy resolution at each energy point. The energy has been reconstructed using the topological cluster reconstruction (4/2/0 σ) and compared with a cone approach for $R = 0.5$. Also shown is the result using the cone cluster reconstruction and applying a 2 σ noise suppression in addition. The fit (lines) is meant to guide the eye only.

in this region. In MC this effect has been taken into account. In general the MC prediction describes the data well, but deviates somewhat from the data in the region of the weak channel.

To better display the details of the shower shape, Fig. 32 shows the same data on logarithmic scale but now for all eight signals. Small deviations of the MC prediction from the data are getting visible on the next-to-next ϕ wedge signals and beyond (MC above data). But these differences are still at a moderate level for the QGSP-BERTINI physics list. This is not so when comparing the data with the GEANT 4 physics list QGSP-GN: here indeed the deviations are somewhat larger yielding a more compact lateral shower distribution.

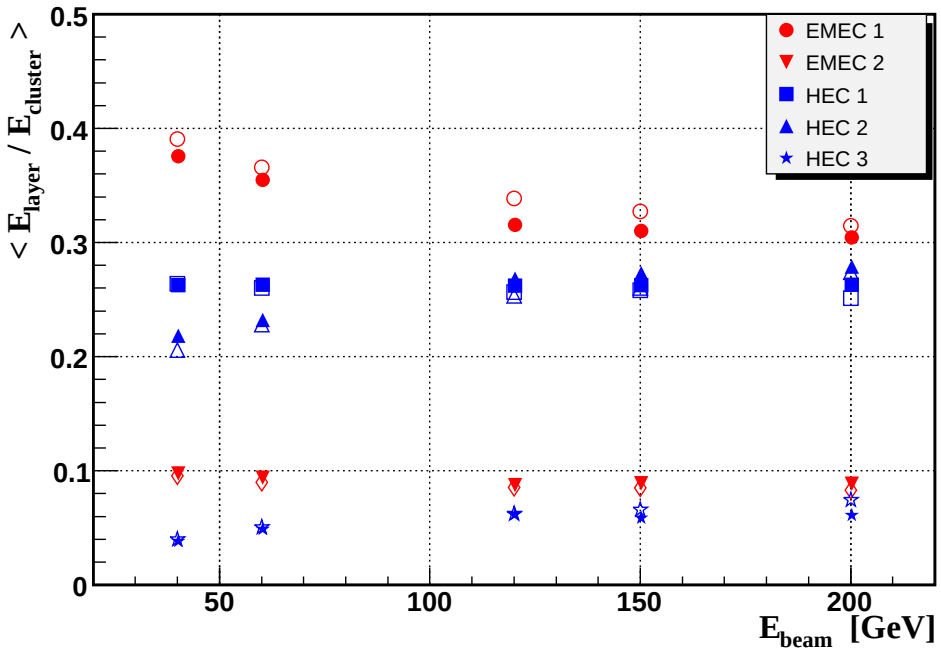

Fig. 30. Longitudinal shower shape for pions with the impact point in EMEC using the electromagnetic scale. Shown is the average cluster energy within a cone of $R = 0.5$ for the various longitudinal sections of the EMEC and HEC as function of energy. The data (full symbols) are compared with the MC prediction (open symbols).

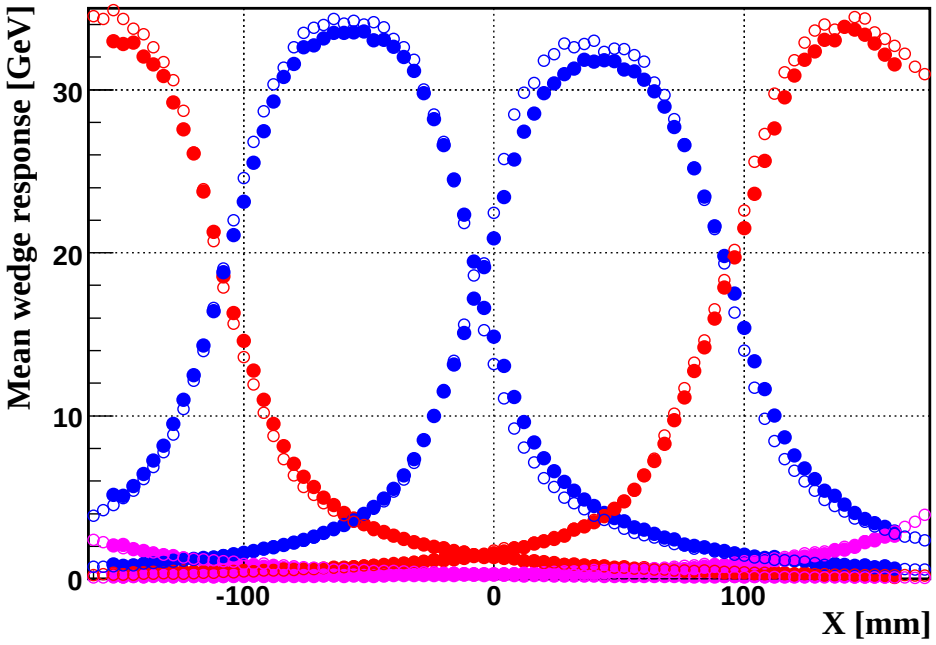

Fig. 31. Lateral shower shape for pions at 60 GeV. Shown is the energy in individual ϕ wedges of $\Delta\phi = 0.2$, integrated in η and summed for the EMEC and HEC calorimeters. At each pion impact point the six relevant contributing signals using the electromagnetic scale are shown for the data (solid points) and MC prediction (GEANT 4 QGSP-BERTINI, open points).

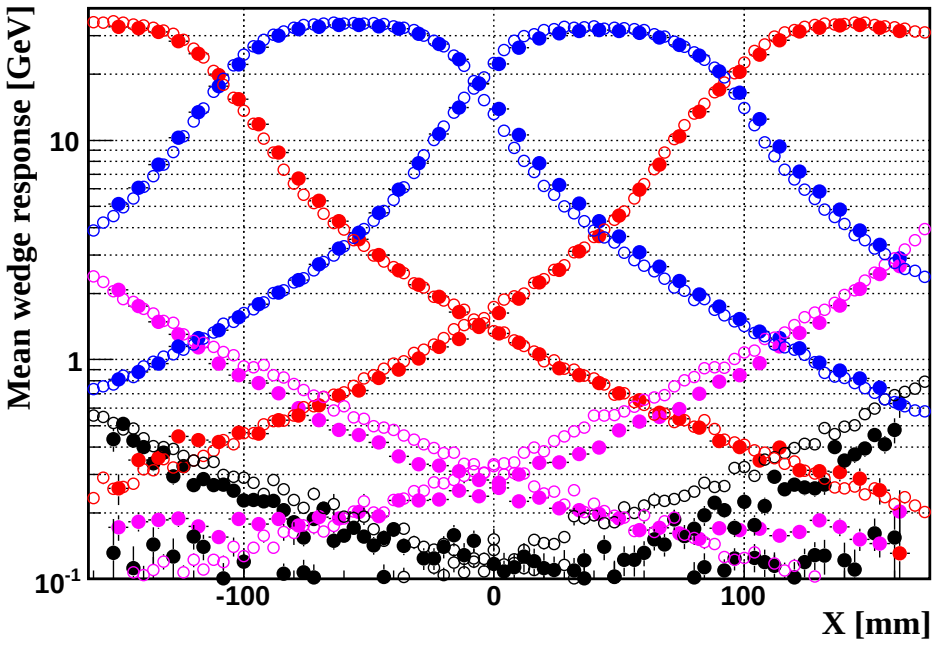

Fig. 32. Lateral shower shape for pions at 60 GeV (logarithmic scale). Shown is the energy in individual ϕ wedges of $\Delta\phi = 0.2$, integrated in η and summed for the EMEC and HEC calorimeters. At each pion impact point the eight contributing signals using the electromagnetic scale are shown for the data (solid points) and MC prediction (GEANT 4 QGSP-BERTINI, open points).

6.4.1 Response on Electromagnetic Scale

The energy dependence of the pion response has also been studied in the FCal region, first using cone reconstructions with $R = 0.3$ and $R = 0.5$, at the electromagnetic scale. Fig. 33 shows the response as function of energy for the impact point H in the FCal (see Fig. 8). The expectations from MC simulations (open points) are shown as well. At lower energies the MC predicts somewhat more energy in a given cone R, but the agreement at higher energies is pretty good. For the larger cone size the effect is reduced. The discrepancy at low energies might be again a consequence of the compact showersize in GEANT4 with the QGSP physics list (see e.g. [18]) . The results of the topological

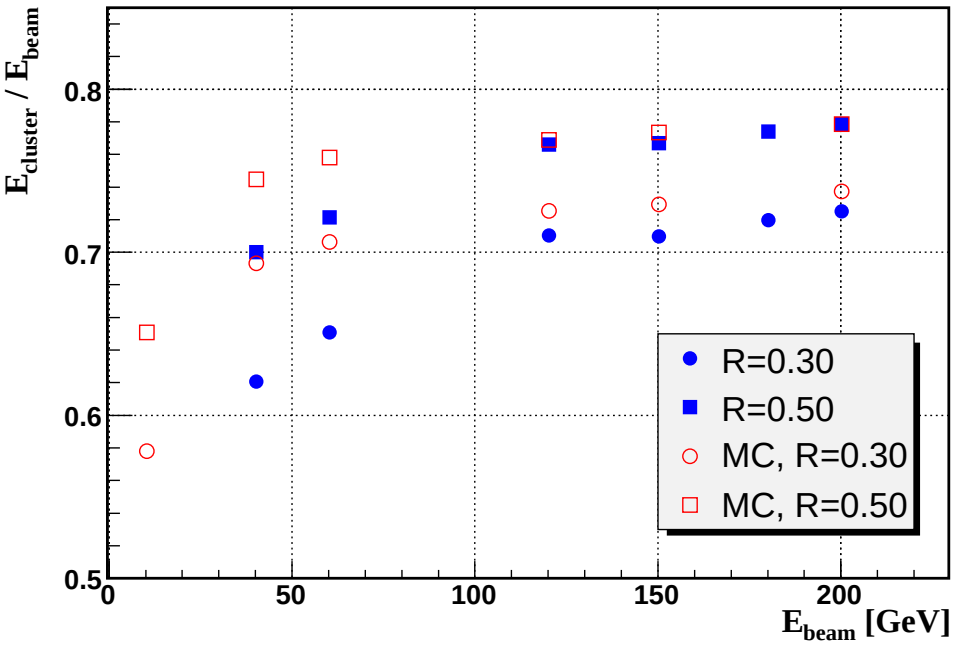

Fig. 33. Energy dependence of the response to pions with the impact point in FCal using the electromagnetic scale (normalized to beam energy). The energy has been reconstructed within a cone of $R = 0.3$ and $R = 0.5$. The expectations from MC simulations (open points) are shown as well.

cluster reconstruction for pions have been compared with those obtained using the cone reconstructions. Again the optimized parameter set 4/2/0 σ was used. Fig. 34 shows the response as function of energy for the 4/2/0 cluster reconstruction. Again, as in the EMEC/HEC region, the response is somewhat lower than for the cone approach ($R = 0.5$), particularly at low energies. But for all energies it is larger than the cone approach in combination with a simple 2 σ noise suppression cut, as expected (see pions in the EMEC/HEC region,

chapter 6.3.1.).

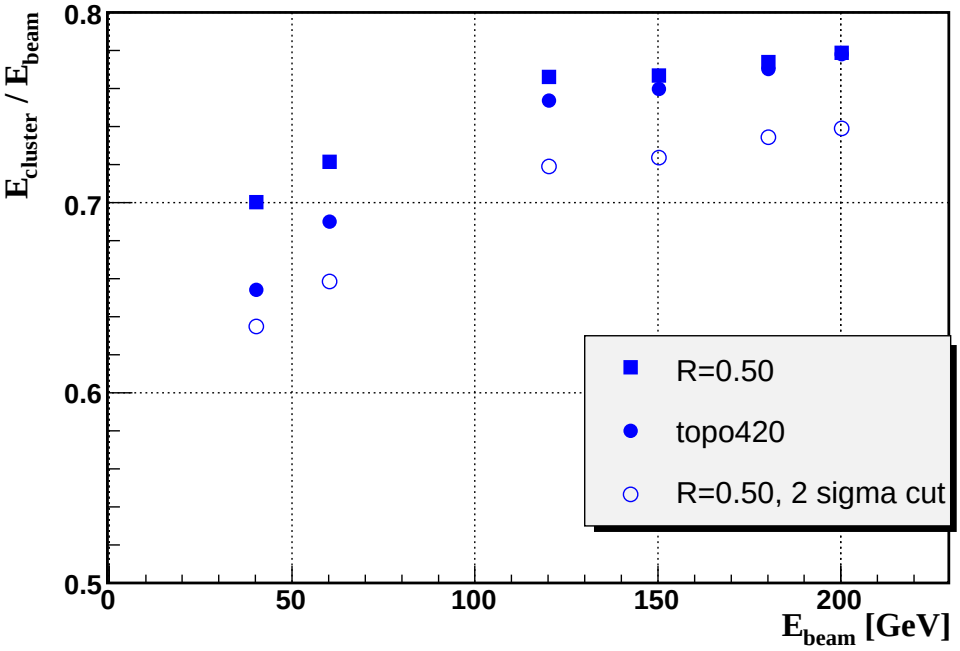

Fig. 34. Energy dependence of the response to pions with the impact point in FCal using the electromagnetic scale. The energy has been reconstructed using the topological cluster reconstruction (4/2/0 σ) and compared with the cone reconstruction ($R = 0.5$). For comparison also the cone reconstruction with an additional 2 σ noise suppression cut is shown as well.

6.4.2 Energy Resolution using the Bench Mark Approach

As for pions in the EMEC/HEC region the data have been compared with MC simulations using the 'bench mark' approach, where one calibration constant per longitudinal section is used. This calibration constant has been obtained by minimizing the energy resolution for each energy point (see pions in the EMEC/HEC region, chapter 6.3.2). Again, for the energy reconstruction cones of $R = 0.3$ and $R = 0.5$ have been assumed. For the two FCal sections the calibration constants follow the weak energy dependence of the e/π ratio in FCAL1 and FCAL2. Fig. 35 shows the energy resolution (full points) as function of energy for the impact point H. The expectations from MC simulations (open points) are shown as well. The noise has been subtracted. The energy resolution expected from the MC simulation (GEANT 4 QGSP-BERTINI) is rather close to the data at high energies. Again, at low energies the MC prediction is somewhat better than what is seen in the data. The resolution has been parameterized using equation (2). The data yield for the larger cone size $R = 0.5$ typically a sampling term of $a = (98.5 \pm 4.0)\,\%\sqrt{\mathrm{GeV}}$

and a constant term $b = (6.4 \pm 0.4)\,\%$ whereas the MC expectations give $a = (74.9 \pm 1.2)\,\%\sqrt{\mathrm{GeV}}$ and a constant term $b = (7.7 \pm 0.1)\,\%$. Again, as was the case for the EMEC/HEC, the difference in the terms is largely driven by the somewhat different energy dependence, yielding a better resolution for the MC at low energies, but being in agreement with the data at high energies. The results obtained are comparable to those obtained in the FCal beam test [8].

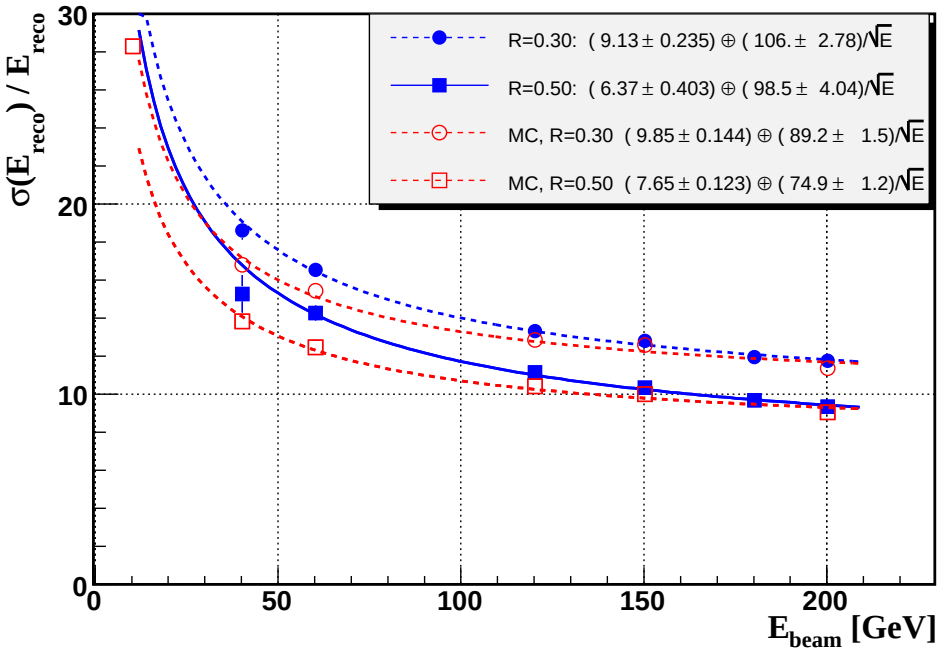

Fig. 35. Energy dependence of the energy resolution for pions with the impact point in FCal, using the 'bench mark' approach. Here one calibration constant per longitudinal section has been determined from a fit minimizing the energy resolution. The energy has been reconstructed within a cone of $R = 0.3$ and $R = 0.5$. The expectations from MC simulations (open points) are shown as well.

The energy dependence of the energy resolution using the topological cluster reconstruction has also been studied. The noise has not been subtracted for these studies. Fig. 36 compares the result for the topological cluster reconstruction with the cone reconstruction ($R = 0.5$) and the cone reconstruction applying a 2 σ noise suppression in addition. Again, the fit to equation (3) using the sampling, constant and noise term, is meant just to guide the eye rather than extract the specific energy resolution parameters. Again the topological cluster reconstruction yields an optimal energy resolution for almost the whole energy range covered, except for the very low energies. This holds also when adding the additional simple noise suppression (2 σ cut) to the normal cone reconstruction ($R = 0.5$).

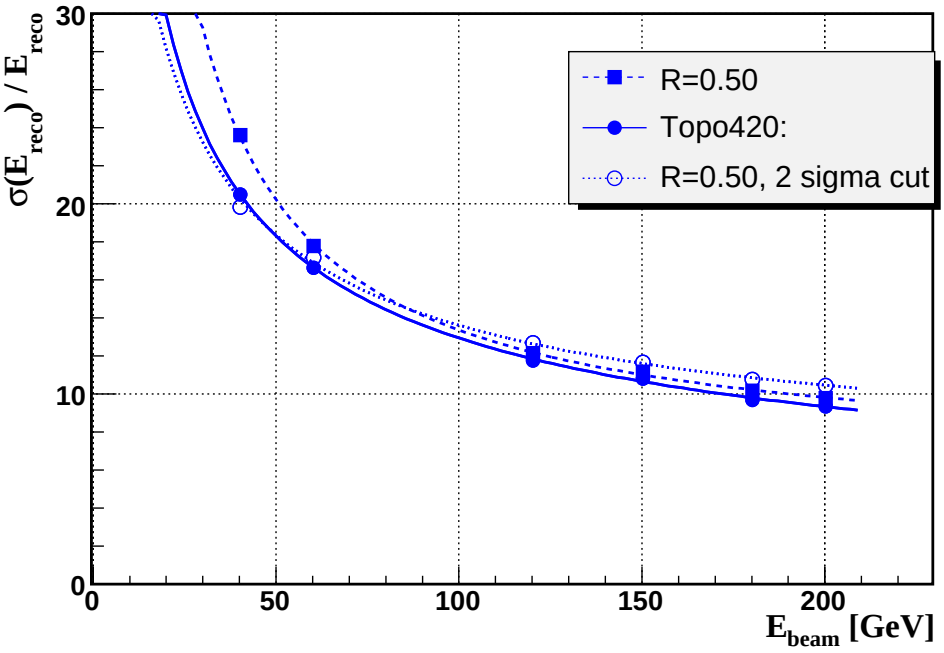

Fig. 36. Energy dependence of the energy resolution for pions with the impact point in FCal using the bench mark approach. Here one calibration constant per longitudinal section has been determined from a fit minimizing the energy resolution at each energy energy point. The energy has been reconstructed using the topological cluster reconstruction and compared with the cone approach ($R = 0.5$) and the cone approach with the additional noise suppression ($2\ \sigma$).

6.5 Discussion of Pion Results

The high granularity of the ATLAS calorimeter and the large number of expected particles per event require a clustering algorithm that is able to suppress noise and pile-up efficiently. Therefore the topo cluster reconstruction is the essential first step in the hadronic calibration. The identification of electromagnetic components within a hadronic cluster using cluster shape variables is the next step in the hadronic calibration procedure. Finally the energy density of individual cells is used to assign the proper weight to correct for the invisible energy deposits of hadrons due to the non-compensating nature of the ATLAS calorimeter and to correct for energy losses in material non instrumented with read-out (e.g. the crack in the region $|\eta| \sim 3.2$ studied in this beam test). The validation of the full hadronic calibration in beam tests will be discussed in a forthcoming paper.

The weighting scheme employs the energy density in individual cells. Therefore the validation of the MC simulation, which is used to define the weighting parameters and energy correction algorithms, is an essential step in the hadronic

calibration procedure. In previous beam test studies (see e.g. [6–9,18]) detailed comparisons of the data with GEANT 3 and GEANT 4 simulations have been carried out. From the various options available, the GEANT 4 QGSP physics list turned out to give the best description of the data. But the agreement was still far from being optimal. In particular the predicted hadronic shower size was too compact when compared with data.

In this analysis we compared the data with GEANT 4 QGSP expectations, but moved on to more recent physics lists like QGSP-BERTINI. Indeed, GEANT 4 QGSP-BERTINI yields a better description of the hadronic shower, reducing the previous shortcomings of the QGSP physics list substantially. But in both regions, EMEC/HEC and FCAL, some residual difference between simulations and data is still visible: the longitudinal and lateral shower shapes point to a still somewhat more compact hadronic shower in MC simulations, eventhough the difference is by far not so large as seen previously with GEANT 4 QGSP simulations. Also the signal response within a given cone is at low energies larger in MC simulations than seen in the data. A smaller cone size enhances this effect even more. Again, this is seen in the EMEC/HEC as well as the FCal region, pointing once more to the different hadronic shower size in MC simulations. With more energy leaking out of the cone in the data with respect to MC simulations, one would expect some discrepancy in energy resolution at low energies. This is indeed observed, again for the EMEC/HEC as well as the FCal region.

A further comparison of the pion data with GEANT 4 simulation, using also different physics lists, will be done in a forthcoming paper.

7 Conclusions

The region of the ATLAS endcap (EMEC/HEC) and forward (FCal) calorimeters in the pseudorapidity range $2.5 < |\eta| < 4.0$ has been studied in beam test runs with electrons and pions. The performance of the EMEC/HEC as well FCal for electrons and pions has been assessed. The results have been compared in detail with MC simulations (GEANT 4). In general, the data show agreement with MC predictions at higher energies. At low energies the GEANT 4 physics list QGSP-GN predicts a somewhat larger pion response (at the electromagnetic scale), coupled with a better energy resolution and more compact shower size than seen in the data. Here QGSP-BERTINI yields a better agreement, in particular for the shower shape. Based on these results, previous studies on the performance of pion and jet reconstruction in ATLAS are substantiated. The full validation of the ATLAS calorimeter reconstruction software will be subject of a forthcoming publication.

Acknowledgements

The support of the CERN staff operating the SPS and the H6 beam line is gratefully acknowledged. We thank the ATLAS-LAr cryogenics operations team and the LAr electronics group for their invaluable help.

This work has been supported by the Bundesministerium für Bildung, Wissenschaft, Forschung und Technologie, Germany, under contract numbers 05 HA 8EX1 6, 05 HA 8UMA 8 and 05 HA 8PXA 2, by the Natural Science and Engineering Research Council of Canada, by the Slovak funding agency VEGA under contract number 2/0061/08 and by ISTC under contract number 1621. We thank all funding agencies for financial support.

References

[1] J. Colas et al., Response Uniformity of the ATLAS Liquid Argon Electromagnetic Calorimeter, Nucl. Instr. and Meth. **A582** (2007) 429.

[2] M. Aharrouche et al., Energy linearity and resolution of the ATLAS electromagnetic barrel calorimeter in an electron test-beam, Nucl. Instr. and Meth. **A568** (2006) 601.

[3] J. Colas et al., Position resolution and particle identification with the ATLAS EM calorimeter, Nucl. Instr. and Meth. **A550** (2005) 96.

[4] B. Aubert et al., Performance of the ATLAS electromagnetic end-cap module 0, Nucl. Instr. and Meth. **A500** (2003) 178.

[5] B. Aubert et al., Performance of the ATLAS electromagnetic barrel module 0, Nucl. Instr. and Meth. **A500** (2003) 202.

[6] B. Dowler et al., Performance of the ATLAS Hadronic End-Cap Calorimeter in Beam Tests, Nucl. Instr. and Meth. **A482** (2002) 94.

[7] D.M. Gingrich et al., Conctruction, Assembly and Testing of the ATLAS Hadronic End-Cap Calorimeter, **JINST 2** (2007) P05005.

[8] Energy Calibration of the ATLAS Liquid Argon Forward Calorimeter, J.P. Archambault et al., accepted by JINST January 2008.

[9] C. Cojocaru et al., Hadronic Calibration of the ATLAS Liquid Argon End-Cap Calorimeter in the Pseudorapidity Region $1.6 < |\eta| < 1.8$ in Beam Tests, Nucl. Instr. and Meth. **A531** (2004) 481.

[10] ATLAS EM end-cap collaboration, Construction, assembly and tests of the ATLAS electromagnetic end-cap calorimeter, to be published in Nucl. Instr. and Meth. **A**.

[11] J. Ban et al., Cold electronics for the liquid argon hadronic end-cap calorimeter of ATLAS, Nucl. Instr. and Meth. **A556** (2006) 158.

[12] The ATLAS Forward Calorimeters, A. Artamonov et al., accepted by JINST January 2008.

[13] S. Simion, Liquid Argon Calorimeter ROD, 2nd ATLAS ROD workshop, October 2000, University of Geneva,
*http : //dpnc.unige.ch/atlas/rod*00*/transp/S_Simion.pdf*.

[14] W.E. Cleland, E.G. Stern, Signal processing consideration for liquid ionization calorimeters in a high rate environment, Nucl. Instr. and Meth. **A338** (1994) 467-497.

[15] L. Kurchaninov, P.Strizenec, Calibration and Ionization Signals in the Hadronic End-Cap Calorimeter of ATLAS, IX International Conference on Calorimetry in High Energy Physics, Annecy, France, 9-14 October, 2000, Frascati Physics Series Vol. XXI, 219-226, 2000.

[16] L. Neukermans, P. Perrodo and R. Zitoun, Understanding the ATLAS electromagnetic barrel pulse shapes and the absolute electronic calibration, ATL-LARG-2001-008.

[17] Marco Delmastro, Energy Reconstruction and Calibration Algorithms for the ATLAS Electromagnetic Calorimeter, PhD thesis, Universita Degli Studi di Milano, 2002, *http : //www.mi.infn.it/ mdelma/physics/phdthesis/*.

[18] A.E. Kiryunin et al., GEANT 4 physics evaluation with testbeam data of the ATLAS hadronic end-cap calorimeter, Nucl. Instr. and Meth. **A560** (2006) 278.

[19] C. Alexa et al., Hadronic Calibration of the ATLAS Calorimeter, 2003, *http://atlas.web.cern.ch/Atlas/GROUPS/LIQARGON/Soft_Cont/Offline/CalibnAlignmnt/index.html*.

[20] S. Agostinelli et al., GEANT 4 - a simulation toolkit, Nucl. Instr. and Meth. **A506** (2003) 250.

[21] C. Serfon, Résultats des tests en faisceau sur les bouchons du calorimètre électromagnétique d'ATLAS, PhD thesis, CPPM Marseille, 3 May 2005.

[22] N. Kerschen, Etude d'un algorithme de reconstruction des electrons dans l'experience ATLAS, PhD thesis DAPNIA-06-21-T, Universite Paris XI, Orsay, 2007.

[23] R. Seuster, Hadronic Calibration of the ATLAS Calorimeter, Proceedings of the XII International Conference on Calorimetry in High Energy Physics, Chicago 2006, APCPC, **867**, 274, (2006).